

UNCLASSIFIED

Penetration Physics of Armor Glass

Donald A. Shockey
Donald R. Curran
Jeffrey W. Simons
Dirk Bermannshoff

SRI International
333 Ravenswood Avenue
Menlo Park, CA 94025-3493

SRI Project P17482

Under Subcontract to:

Southwest Research Institute
P.O. Drawer 28510
San Antonio, TX 78238

Prime Contract: W56HZV-06-C-0194

SwRI[®] Report 18.12544/019

Prepared for:

US Army RDECOM-TARDEC
AMSRD-TAR-R
Warren, MI 43897-5000

November 2009

UNCLASSIFIED

UNCLASSIFIED

UNCLASSIFIED

REPORT DOCUMENTATION PAGE				<i>Form Approved</i> OMB No. 0704-0188	
Public reporting burden for this collection of information is estimated to average 1 hour per response, including the time for reviewing instructions, searching data sources, gathering and maintaining the data needed, and completing and reviewing the collection of information. Send comments regarding this burden estimate or any other aspect of this collection of information, including suggestions for reducing this burden to Washington Headquarters Service, Directorate for Information Operations and Reports, 1215 Jefferson Davis Highway, Suite 1204, Arlington, VA 22202-4302, and to the Office of Management and Budget, Paperwork Reduction Project (0704-0188) Washington, DC 20503.					
PLEASE DO NOT RETURN YOUR FORM TO THE ABOVE ADDRESS.					
1. REPORT DATE (DD-MM-YYYY) 30-11-2009		2. REPORT TYPE Technical		3. DATES COVERED (From - To) July 31, 2006 – June 30, 2009	
4. TITLE AND SUBTITLE Penetration Physics of Armor Glass				5a. CONTRACT NUMBER W56HZV-06-C-0194	
				5b. GRANT NUMBER	
				5c. PROGRAM ELEMENT NUMBER	
				5d. PROJECT NUMBER	
6. AUTHOR(S) Donald A. Shockey, Donald R. Curran, Jeffrey W. Simons, Dirk Bergmannshoff				5e. TASK NUMBER	
				5f. WORK UNIT NUMBER	
7. PERFORMING ORGANIZATION NAME(S) AND ADDRESS(ES) SRI International 333 Ravenswood Avenue Menlo Park, CA 94025-3493				8. PERFORMING ORGANIZATION REPORT NUMBER SRI: P17482 SwRI: 18.12544/019	
9. SPONSORING/MONITORING AGENCY NAME(S) AND ADDRESS(ES) US Army Tank-Automotive Research, Development, and Engineering Center, Warren, MI 48397-5000				10. SPONSOR/MONITOR'S ACRONYM(S) RDECOM-TARDEC	
				11. SPONSORING/MONITORING AGENCY REPORT NUMBER	
12. DISTRIBUTION AVAILABILITY STATEMENT Approved for Public Release; Unlimited Distribution					
13. SUPPLEMENTARY NOTES Performed under subcontract to Southwest Research Institute, P.O. Drawer 28510, San Antonio, TX 78238. The views, opinion, and/or findings contained in this report are those of the authors and should not be construed as an official Department of the Army position, policy, or decision, unless so designated by other documents.					
14. ABSTRACT As part of a team working to develop improved ceramic and glass armor, SRI International performed and interpreted experiments designed to elucidate the physics of material failure when attacked by a rod-like projectile. Partially penetrated glass targets were sectioned and examined to observe the fracture damage. Finely comminuted material in advance of arrested penetrators suggested that frictional properties of fragments influence penetration. A test was devised and applied to measure shear resistance of a bed of fragments at high pressure. The results formed the basis for a physics-based model of fracture and flow of glass ahead of a penetrator and, hence, the basis for computational simulations of projectile/armor encounters that can be used for armor design. The partial penetration experiments and findings are described in Section III, and the mesomodel of glass fracture and flow is presented in Section IV. All three sections were presented at meetings of the American Ceramic Society and all were reviewed and published in the proceedings.					
15. SUBJECT TERMS glass armor, Mescall zone, humvee window, penetration physics, shear resistance, partial penetration experiment, fragment flow					
16. SECURITY CLASSIFICATION OF:			17. LIMITATION OF ABSTRACT None	18. NUMBER OF PAGES 42	19a. NAME OF RESPONSIBLE PERSON Dr. Douglas Templeton
a. REPORT Unclassified	b. ABSTRACT Unclassified	c. THIS PAGE Unclassified			19b. TELEPHONE NUMBER (Include area code) 586-574-5325

UNCLASSIFIED

UNCLASSIFIED

Table of Contents

	Page
SECTION I: Introduction and Summary	1
SECTION II: Physics of Glass Failure During Rod Penetration	3
Abstract	3
Introduction	3
Partial Penetration Experiments	3
Damage Observations	5
Projectile Damage	10
Discussion	11
Summary	13
Acknowledgements	13
References	13
SECTION III: Flow Behavior of Glass at the Tip of a Penetrator	15
Abstract	15
Introduction	15
Experimental	16
Results	17
Post-Test Specimen Examination	18
Discussion	21
Summary	22
Acknowledgements	22
References	22
SECTION IV: Mesomechanical Constitutive Relations for Glass and Ceramic Armor	23
Abstract	23
Background and Program Goals	23
Mesomechanical Approach	23
Conceptual Mesomechanical Model	24
Supporting Experiments	27
Uniaxial strain plate impact response	27
Partial penetration of non-eroding rods	31
Future Test Program	32
Partial penetration tests	32
Quasistatic property tests	32
Soft-recovered plate impact tests	32
Conclusions	33
Acknowledgements	34
References	34

UNCLASSIFIED

List of Figures

	Page
SECTION II: Physics of Glass Failure During Rod Penetration	3
Figure 1. Target assembly before and after impact	4
Figure 2. Section through target showing damage around impact site	5
Figure 3. Off-center section showing in-situ fragments formed by intersecting cone and lateral cracks	6
Figure 4. Thin petrographic section showing fragment colonies, individual fragment shapes, and fragment packing pattern in the tunnel surrounding the projectile	7
Figure 5. Closely-spaced cone cracks beneath the nose of an arrested projectile	8
Figure 6. Agglomerated glass fragments attached to a projectile	8
Figure 7. Size distribution of fragments in the $< 30 \mu\text{m}$ at four locations within the tunnel of a partially penetrated target	9
Figure 8. Glass fragments collected from a projectile tunnel	9
Figure 9. Scoring marks on recovered projectile (a) and on nose (b)	10
Figure 10. Melting evidence on the glass layer adhering to the projectile nose (a) and on a glass surface that was adjacent to the projectile shaft (b)	10
Figure 11. Stress conditions and damage activity ahead of a penetrating projectile	11
Figure 12. Strength of intact and comminuted glass and the stress path experienced by glass during penetration	12
SECTION III: Flow Behavior of Glass at the Tip of a Penetrator	15
Figure 1. Specimen, holding jig, and loading mode for compressing and shearing glass powder	16
Figure 2. Shear stress vs. shear strain as a function of pressure	17
Figure 3. (a) Quartz powder after 200 kN compression followed by shear. (b) Quartz powder after 200 kN compression only	18

List of Figures (Cont'd)

	Page
Figure 4. Size distribution of 3.5 μm quartz glass powder after testing at normal loads of 10 kN, 50 kN, and 200 kN (normal stresses of 69 MPa, 342 MPa and 1.37 GPa)	19
Figure 5. Polished cross section normal to the specimen radial direction showing cracks	19
Figure 6. Surface of glass specimen next to steel anvil showing smear markings and interface stick/slip evidence	20
SECTION IV: Mesomechanical Constitutive Relations for Glass and Ceramic Armor	23
Figure 1. Schematic picture of conceptual mesomodel	25
Figure 2. Postulated CMM yield behavior.....	26
Figure 3. Wing Crack.....	27
Figure 4. Comparison of CMM model trends with simplified Simha & Gupta data. Measurement is 3 mm from impact surface	31
Figure 5. Plate impact test design	33
Table 1. Properties for SLG and B4C	28

SECTION I: INTRODUCTION AND SUMMARY

A goal of the Army is to improve the ballistic performance of windows in humvees and military vehicles. Current windows are made of glass and can be 10 cm thick and weigh 40 Kg. The weight of 6 windows, equivalent to 2 or 3 soldiers, wears out suspension systems and transmissions. Alternative transparent materials such as ALON, spinel, and sapphire could provide the required ballistic protection at considerably less weight, but are considerably more expensive and hence less attractive. Thus, glass is the material of choice for Army vehicles.

Windows are typically laminated structures and are designed empirically. The number and thicknesses of the glass layers, the type and thickness of adhesive, etc. are chosen, and the windows are manufactured and evaluated in ballistic tests. Then the test results are noted, structural parameters are adjusted, and another series of ballistic tests is performed. The process is repeated. This iterative empirical approach has produced windows that have functioned well. However, the product is likely not optimal. Continued "shoot and see" experiments may not produce significant improvements, even with considerable expense and time investment.

An alternative approach is to determine the mechanism of glass failure when attacked by a projectile. Insight gained would then be used to suggest changes in the glass microstructure or changes in the armor window macrostructure that disrupt this mechanism and hence lead to a better product. The research effort reported here takes this more scientific approach.

The process by which a rod penetrates glass was investigated by examining the fracture damage in a partially penetrated target block. Projectiles of different sizes, shapes, and materials were accelerated against monolithic and laminated glass targets at velocities sufficient to penetrate part way through the target thickness. The cracked targets were held in place by infiltrating with a low-viscosity, quick-setting, two-component epoxy and then sectioned with a diamond saw usually on a plane through the shot line. The surfaces of section were then polished and examined with optical and scanning electron microscopy to observe the extent and pattern of cracking, and the size and shapes of fragments.

All targets showed cone cracks, radial cracks, ring cracks, and lateral cracks typical of particle or rod impact. A cylindrically "tunnel" of glass fragments about 1 to 3 projectile radii in diameter surrounds the embedded projectile, an uplifted "lip" of material is produced at the impact surface, and a "Mescall zone" of highly comminuted material exists at the tip of the arrested penetrator. It is this comminuted material that must move out of the path of the projectile for the projectile to advance. The partial penetration experiments and findings were presented at the 2008 meeting of the American Ceramic Society and published in the proceedings; they are described in Section II of this report.

The picture that emerges from these experiments is that target material at the leading edge of the projectile is transformed to powder, which then is extruded to the side into the tunnel region and subsequently flows opposite the penetration direction and out the front surface. Thus, the flow characteristics of these fine fragments control penetration and, hence, the performance of the armor.

The opportunity and the challenge of armor developers is thus to understand, model, and find ways to inhibit this flow. The quest was begun in this project. A laboratory test was designed and applied to measure the shear resistance of a fragment bed under high pressure. The procedure and results were presented at the 2009 meeting of the American Ceramic Society and was published in the proceedings; they are described in Section III of this report.

Finally, we constructed a model based on observations and data from the partial penetration experiments and fragment flow tests. The model treats microdamage evolution, i.e., the nucleation, growth, and coalescence of microcracks in the Mescall zone, and subsequent granular flow of the comminuted material out of the path of the advancing penetrator. The goal is to relate material failure on the microscopic level to continuum behavior, and to give guidance to continuum models used in hydrocodes for designing transparent armor.

Section IV describes a proposed initial framework for the mesomodel, incorporates available data, discusses preliminary correlations of predictions with observations, and discusses future proposed experiments. This work was presented at the 2008 meeting of the American Ceramic Society and was published in the proceedings.

SECTION II: PHYSICS OF GLASS FAILURE DURING ROD PENETRATION

D. A. Shockey, D. Bergmannshoff, D. R. Curran, and J. W. Simons
SRI International, Menlo Park, CA 94025

ABSTRACT

The failure physics of glass when attacked by a projectile was investigated by examining the damage in glass target blocks that were partially penetrated by a steel rod. Fragment shapes and sizes in the tunnel surrounding embedded projectiles suggest penetration occurs by comminution of material at the nose of the advancing projectile and subsequent flow of the fine fragments out of the projectile path into more coarsely fragmented tunnel material. The observations and measurements are being used to develop a physics-based model that enables computational simulations of glass penetration scenarios and design of transparent armor.

INTRODUCTION

A goal of the Army is to reduce the weight of vehicle windows while meeting ballistic performance requirements. Current efforts to determine appropriate trade-offs between protection and weight are mostly experimental, where windows of different materials and structure are fabricated and then subjected to ballistic tests. Trade-offs can be examined more quickly and at lower expense with computational simulations, but the reliability and the detail of the computation results depend on how well the constitutive equations describe material failure behavior. Models deduced by fitting computational results to depths-of-penetration observed in ballistic tests do not always predict behavior in another impact scenario (see for example References 1-3), nor do they always compute certain features of interest, such as dwell time or the extent of damage. The ability of a window to survive a second impact, for example, requires that damage and strength loss associated with the first impact be modeled. For such purposes, a material model based on the failure physics of glass during penetration is needed.

To generate such a model, an understanding of the mechanism of penetration is required, as is a quantitative description of the damage. Our approach to obtain this information is to (1) perform ballistic experiments on glass targets at velocities such that the projectile penetrates only partially through the glass, (2) examine the targets post-test, and (3) characterize and quantify the damage.

PARTIAL PENETRATION EXPERIMENTS

Partial penetration of glass target blocks was achieved by accelerating steel rods to velocities in the 300 to 600 m/s range with a .458 magnum rifle. The projectile rods, which weighed 7.5 grams, were fitted in standard .458 shells with 3.4-gram sabots made of Delrin. The quantity of powder charge was adjusted to achieve desired velocities and a powder weight-projectile velocity calibration curve was determined in a series of gun firings.

Projectile rods 31.75 mm long and 6.35 mm in diameter with a hemispherical nose were machined from 6.35 mm maraging steel rod. The rods were heat soaked at 482°C for 6 hours, then slowly cooled to achieve a hardness of R_C 52. Mechanical properties

were not measured, but in this heat-treat condition the projectiles should have yield and ultimate tensile strengths of 1780 MPa and 1850 MPa, respectively.

Targets of soda lime glass 100x100x50 mm and borosilicate glass 195x195x75 mm were encased front and back with 9-mm-thick PMMA plates, and on the sides with a PMMA “picture frame” to contain the fractured target after ingress of the projectile. The cover plates had a central hole to allow the impacting rod to hit only glass. Velocities of 300 to 600 m/s produced depths of penetration from 10 to 23 mm; therefore the nose of the arrested penetrator was 40 mm or more from the rear surface of the glass target. Several targets cracked through and the penetrator lay separated from the target pieces. The slightly tilted attitude of the arrested projectile suggested some yaw at impact. Figure 1 shows a target before and after impact.

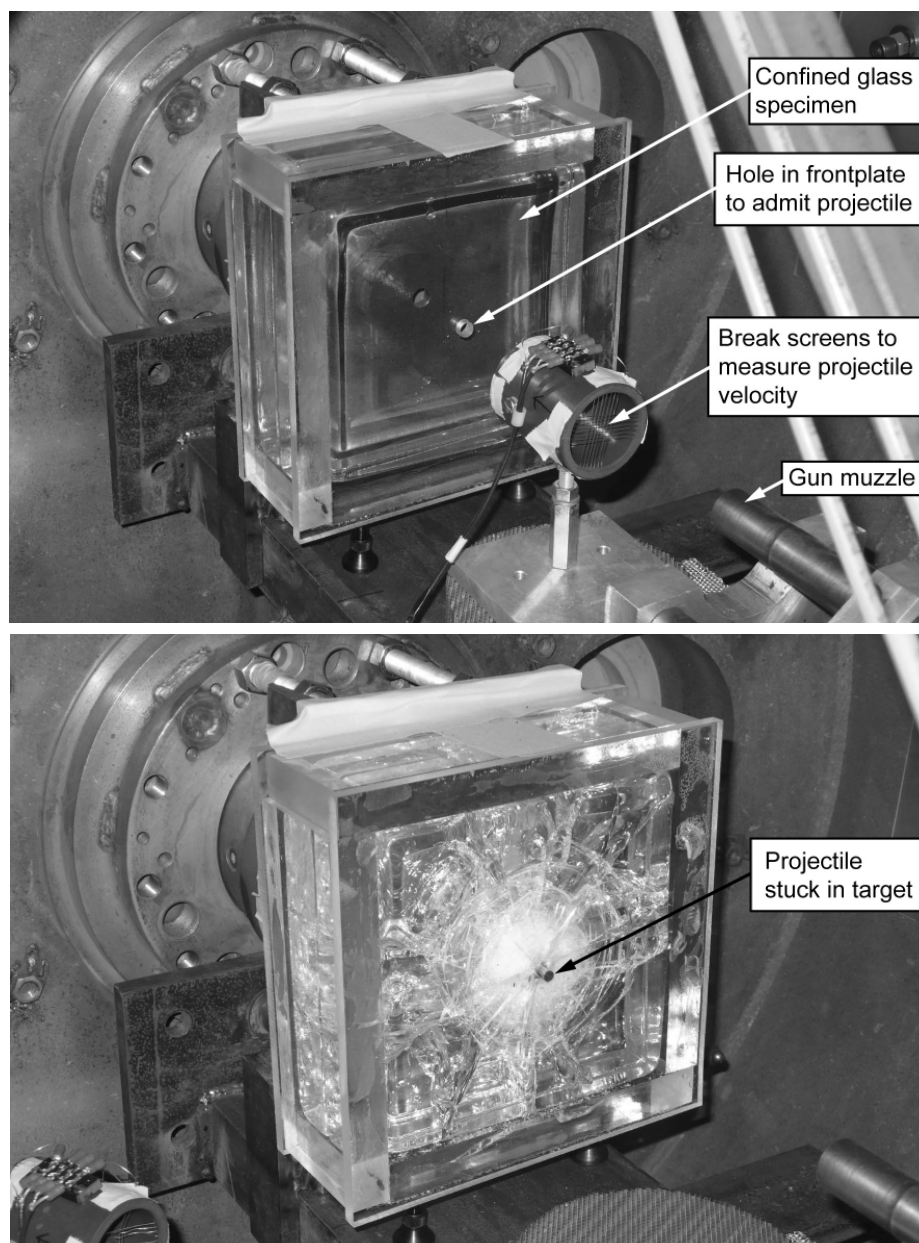


Figure 1. Target assembly before and after impact.

After the impact, the encased targets with the embedded projectiles were carefully removed from the target mount to minimize shifting of the glass fragments, placed in the heated vacuum chamber on the rear plate (face plate up), and infiltrated with epoxy to hold the fragments in place and allow the fragmented target to be sectioned. A low-viscosity epoxy was poured into the front plate hole and the pouring chamber was evacuated overnight. The next day the target was inverted, the rear plate was removed, and the infiltration procedure was repeated for the rear target surface. After the targets were stabilized, the remaining confinement was removed and the targets were cut in two on a plane that included the penetration axis. Several targets were not stabilized with epoxy in order to collect loose fragments or compacted agglomerates for size distribution analysis.

DAMAGE OBSERVATIONS

The cross sections through the shot line revealed the uplifted target material near the impact site, the well-known cone and lateral cracks⁴⁻⁹, and a concentric white frosted region around the projectile cavity, figure 2. The boundary between this white region and the more transparent region defines the tunnel. For the conditions of these experiments, the tunnel boundary (outer radius) is about 4 to 12 mm from the penetrator center line, or about 1 to 4 projectile radii.

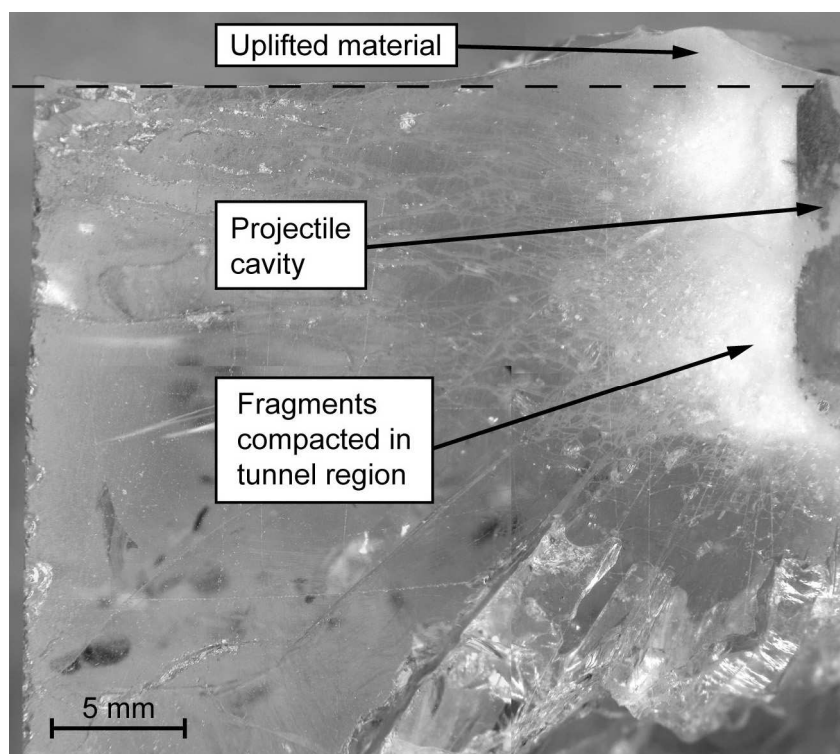


Figure 2. Section through target showing damage around impact site.

Similar cross sections near the nose of the arrested projectile but taken one projectile diameter from the shot line, Figure 3, show the cracking pattern and in-situ fragments, possibly illustrating how tunnel fragments form. Closely spaced (about 0.3-0.5 mm apart) cone cracks fan out in a divergent pattern and the long slender strips of glass between them are segmented by lateral cracks, producing rectangular fragments with aspect ratios ranging from 1 to 4.

Figure 4, a petrographic thin section parallel to the cross section in Figure 2, provides a clearer look at material in and around the tunnel (the circular white areas are air bubbles trapped during preparation of the thin sections). The transparent material at some distance from the projectile cavity in Figure 2 is heavily cracked and fragmented, but the fragments are in their original positions relative to each other. The white frosted region is more densely cracked and more finely fragmented. Moreover, the fragments have moved and rotated from their original positions. The boundary between the coarsely and finely fragmented regions is the boundary of the tunnel.

The densely cracked tunnel consists of colonies of in-situ fragments in a matrix of smaller, more randomly-oriented fragments. These colonies are nominally equiaxed with diameters up to 1 mm. In-situ fragments within the colonies are rectangular with aspect ratios of about 1 to 4, defined by perpendicular intersecting cone and lateral cracks. The orientation of the cone cracks within a colony with respect to the cone cracks outside the tunnel attests to rotation of the colony as the projectile penetrated.

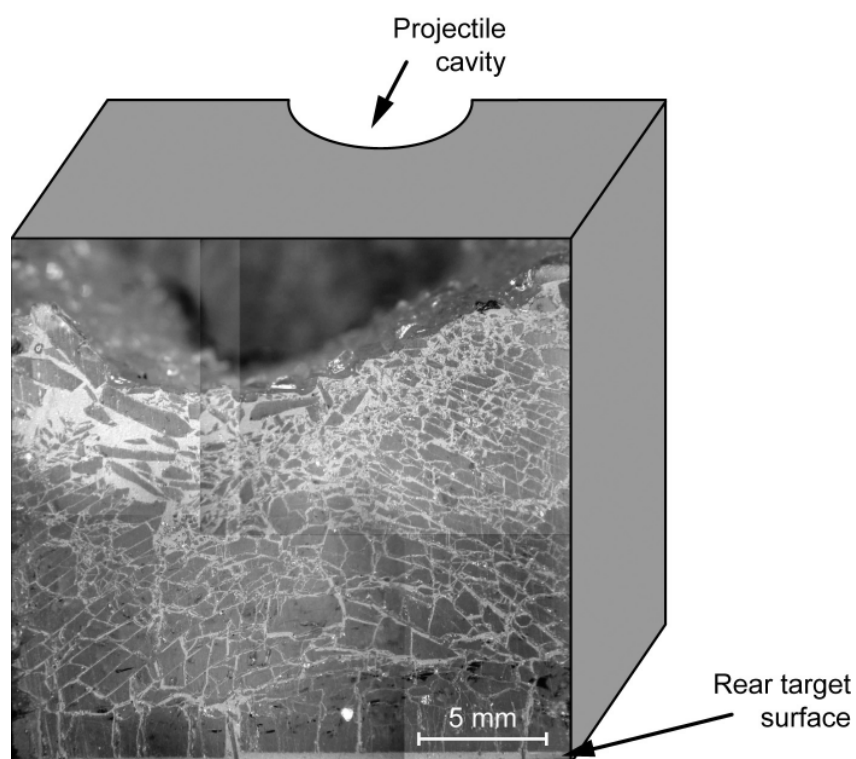


Figure 3. Off-center section showing in-situ fragments formed by intersecting cone and lateral cracks.

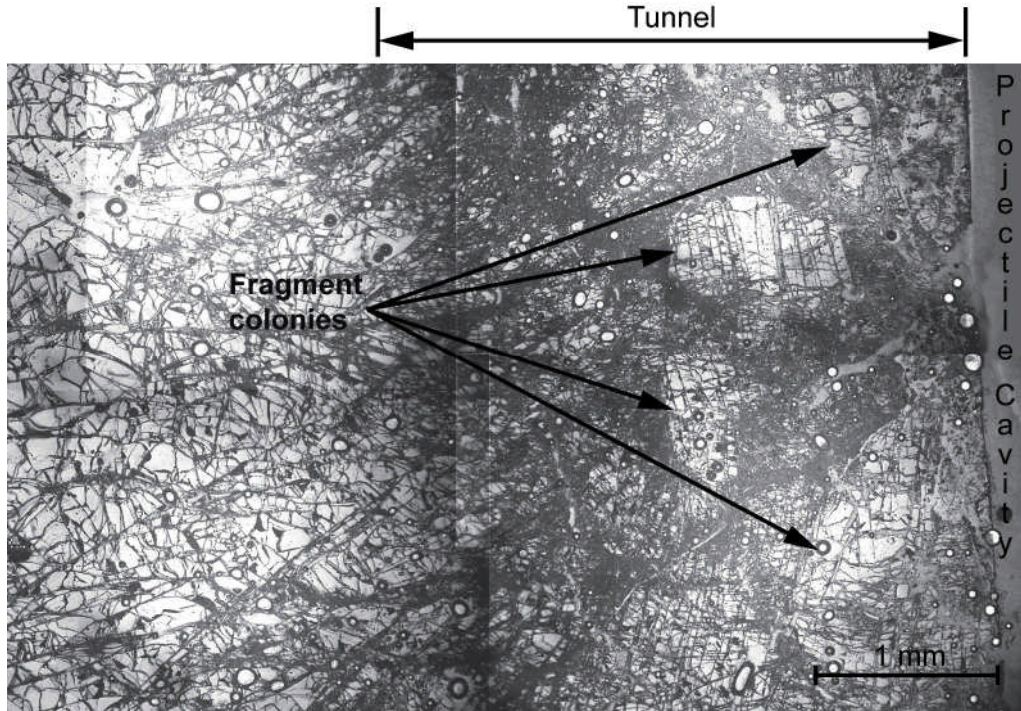


Figure 4. Thin petrographic section showing fragment colonies, individual fragment shapes, and fragment packing pattern in the tunnel surrounding the projectile.

Beneath the arrested projectile tip were closely-spaced cone cracks extending in the penetration direction, Figure 5. Little evidence of the Mescall zone* (MZ),^{10,11} the highly stressed, finely comminuted volume of target directly beneath the nose of an advancing projectile, could be observed, because an arresting projectile does not produce high-shear stresses and, hence, does not produce the damage representative of a fast-moving projectile. However, small rounded fragments mixed in with the large angular fragments in the tunnel may be MZ fragments produced by a fast-moving projectile that have migrated away from the MZ.

* Named for John Mescall who first deduced its existence.^{12,13}

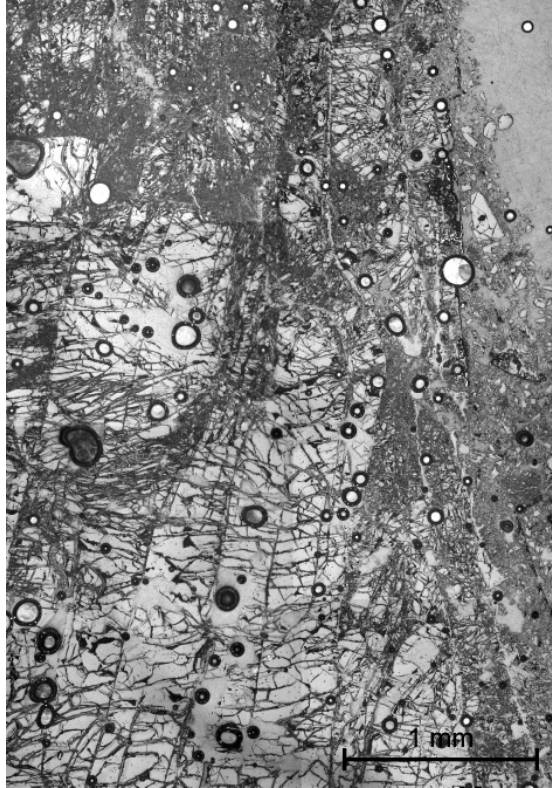


Figure 5. Closely-spaced cone cracks beneath the nose of an arrested projectile.

The fragments in the tunnel are firmly compacted. For tests in which the glass targets cracked through, the projectile was not embedded, but was found lying in the test chamber with the tightly compressed tunnel material attached, Figure 6. This provided an opportunity to measure the fragment size distribution of tunnel material.

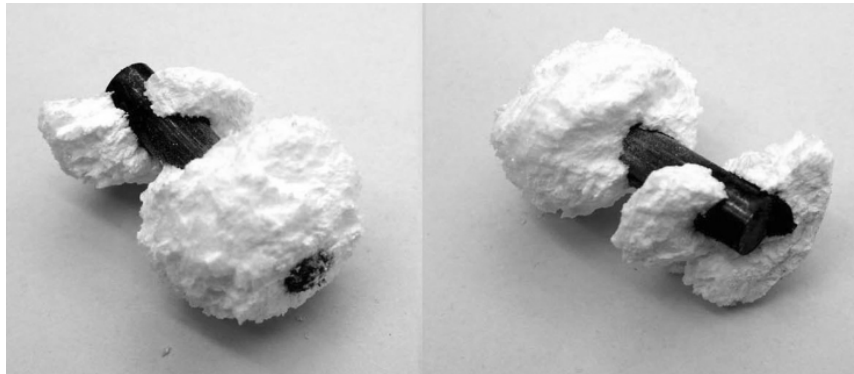


Figure 6. Agglomerated glass fragments attached to a projectile.

Samples of this coherent glass powder agglomerate were taken from four locations: at the nose and half-shaft position of the penetrator and near the inside and outside boundaries of the tunnel. Triplicate measurements of fragment radius distribution in the range up to 120 microns were made at each location with a Horiba particle classifier. Figure 7 shows the size distribution of fragments having radii up to 30 microns.

Fragment radii showed little variation with position in the tunnel. Figure 8 shows that the larger fragments are cube-like, bar-like, and plate-like with sharp edges and corners, having aspect ratios of 1 to 4. A few large (0.2 to 0.5 mm) fragment colonies, such as seen in Figure 4, were embedded in the agglomerate.

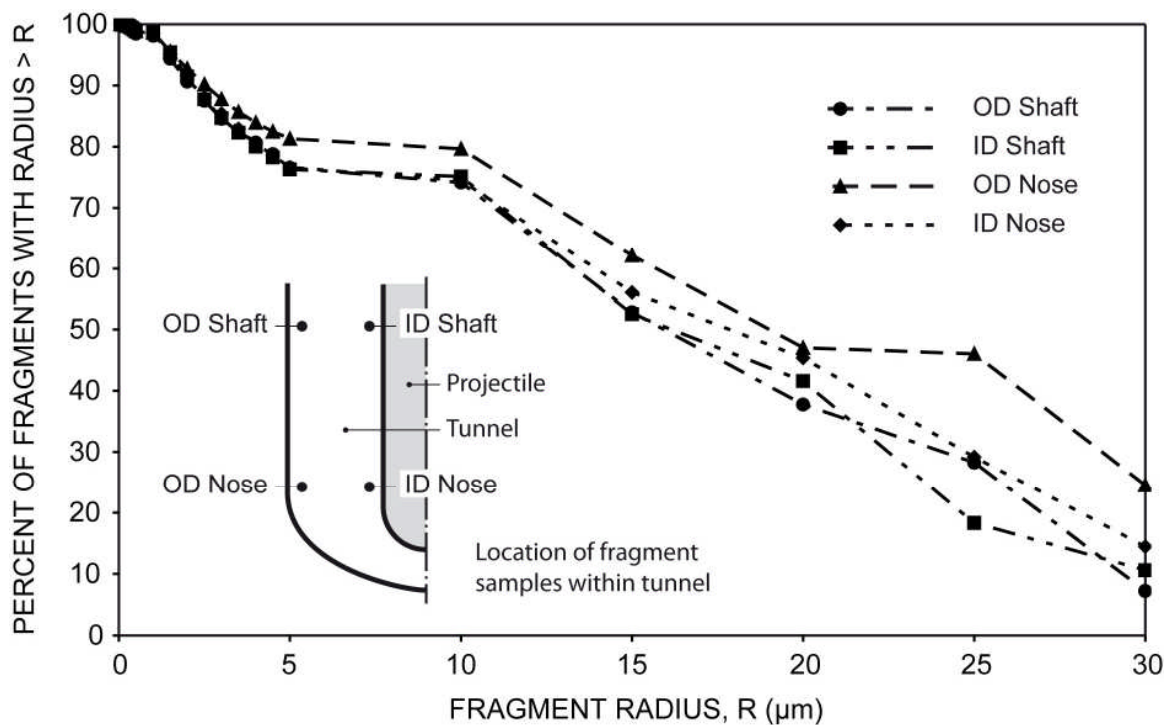


Figure 7. Size distribution of fragments in the < 30 μm at four locations within the tunnel of a partially penetrated target.

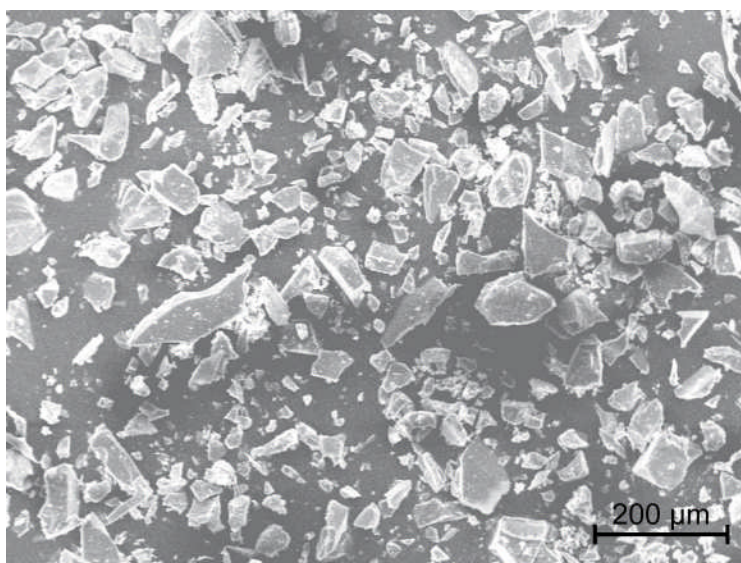


Figure 8. Glass fragments collected from a projectile tunnel.

PROJECTILE DAMAGE

Projectiles recovered after impact had axial grooves along the embedded portion of their shafts and a layer of glass attached to their noses, Figure 9(a). Patches of parallel grooves were evident on the projectile nose when the adherent glass layer was removed, Figure 9(b). The grooves attest to the abrasive effect of glass fragments as the projectile advances in the target.

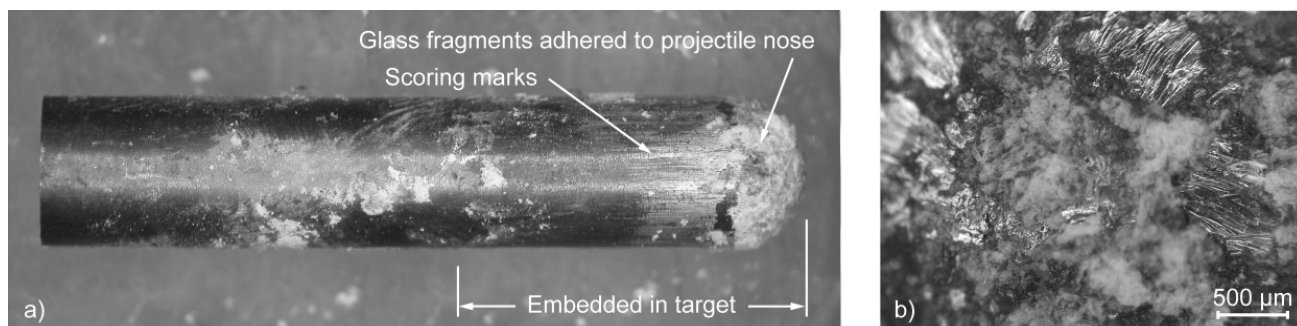


Figure 9. Scoring marks on recovered projectile (a) and on nose (b).

Close examination of the glass layer on the projectile nose, Figure 10(a) shows smeared areas that have cracked, suggesting that the high pressure and the interfragment friction generate enough heat to soften and perhaps melt glass fragments. Surfaces that were in contact with the projectile shaft during penetration exhibit small glass globules and lines of globules, Figure 10(b). Petrographic thin sections such as shown in Figure 4 also suggest that a thin layer of fused glass may exist next to the projectile.

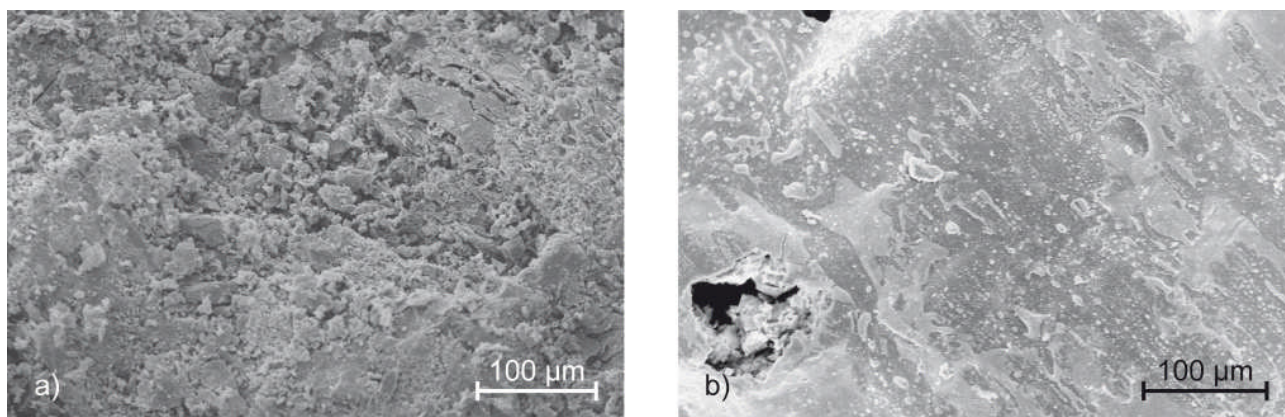


Figure 10. Melting evidence on the glass layer adhering to the projectile nose (a) and on a glass surface that was adjacent to the projectile shaft (b).

The surface of the fragment agglomerate in contact with the projectile shaft in Figure 6 was blackened and coherent, suggesting frictional heating and chemical interaction between projectile and target. Chemical analysis of this surface showed iron, nickel, titanium, and molybdenum, the main constituents of the maraging steel projectile and in approximately the same percentage. Analysis of the agglomerate further from the

projectile showed none of these elements. Thus, the projectile was slightly eroded thermally, chemically, and mechanically as it penetrated the glass target.

DISCUSSION

These observations suggest that penetration occurs by comminution of glass in the Mescall zone ahead of the projectile nose and the extrusion of the fine glass fragments out of the projectile path and into a more coarsely fragmented “tunnel” region surrounding the projectile. The cracking and fragment patterns are consistent with three distinct stress zones around the projectile, Figure 11. A material particle ahead of the projectile is loaded, damaged, and displaced in three successive steps under consecutive tensile, shear, and compressive stress states, as shown schematically in Figure 12.

The material initially experiences tension, and acquires closely-spaced cone cracks running at slight radial angles to the penetration direction, Zone 1. Subsequent lateral cracks break up the material between adjacent cone cracks. Next, as the projectile moves closer, a local volume (about the size of the projectile nose) of this cracked material is overrun by a low-confinement field of high shear and is comminuted into fine fragments, Zone 2. Thirdly, the projectile reaches the comminuted material and imposes high pressure, Zone 3, extruding the comminuted material to the sides of the projectile nose and into the cracked and coarsely fragmented tunnel.

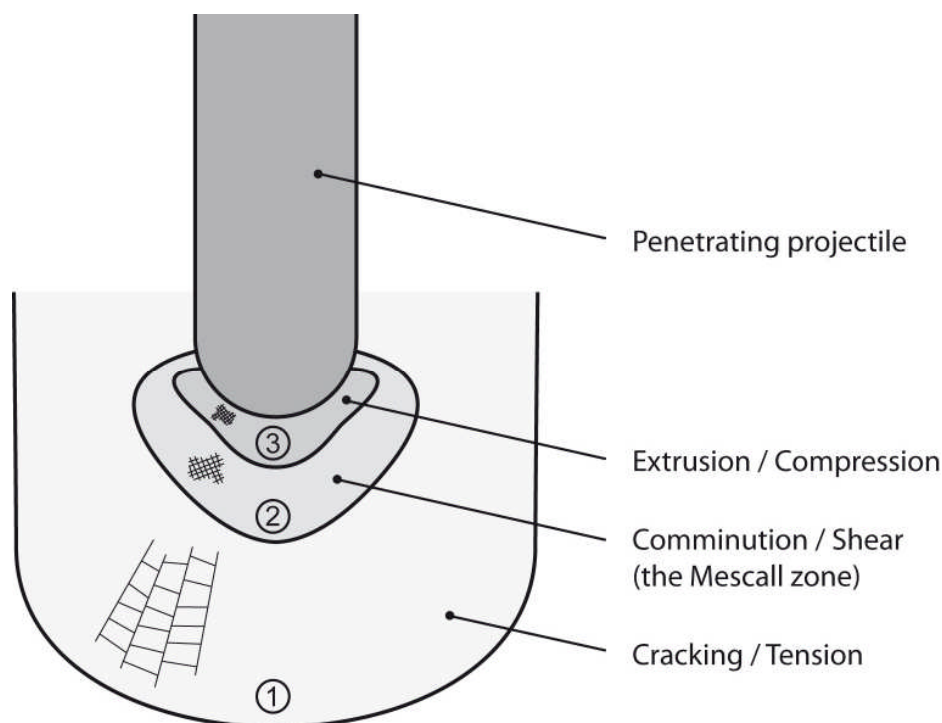


Figure 11. Stress conditions and damage activity ahead of a penetrating projectile.

Target material displaced by the projectile is accommodated in the early stages of penetration by ejection of target fragments and uplift at the impact surface. At later stages, the flow of fragments is probably primarily in the radial direction, a flow accommodated by favorably oriented macrocracks in the tunnel, which are wedged apart to provide paths for migrating MZ material. Flow may be facilitated by frictional heat

generated during penetration, which may soften or melt glass fragments, and by the slight rotation of colonies of cracked tunnel material.

Since target material must flow out of the path of the projectile for the projectile to advance, microcracking in the MZ is the key underlying mechanism governing penetration. The intensity of MZ microcracking dictates MZ fragment size and shape, which in turn dictate flow behavior. Thus, microcrack numbers, sizes, spacings, and orientations in the MZ are necessary data for failure physics models of penetration. Although posttest damage is not representative of dynamic processes occurring ahead of a projectile, quantitative estimates of microcrack size and density in the MZ may be obtained from the sizes and shapes of MZ fragments in the tunnel region. MZ fragments should be distinguishable from fragments that formed in the tunnel. They should be smaller than tunnel fragments, because they form under higher compression and shear conditions. Moreover, they should be less angular than tunnel fragments, since they probably rotate and rub edges off as they flow out of the MZ and, further, may have softened under compressional and frictional heat.

Future work is aimed at modeling MZ microfracture activity, a task that requires identifying MZ fragments among the fragments in the tunnel and measuring their size distribution. The MZ fragment size distribution will be analyzed to obtain estimates of MZ microcrack numbers and sizes. Laboratory tests will be performed to measure frictional flow properties of fragment beds, i.e., shear strength as a function of pressure. These data will be used to develop a computational model of rod penetration into glass. The framework of this fracture-physics-based model is presented in a paper which follows¹⁴.

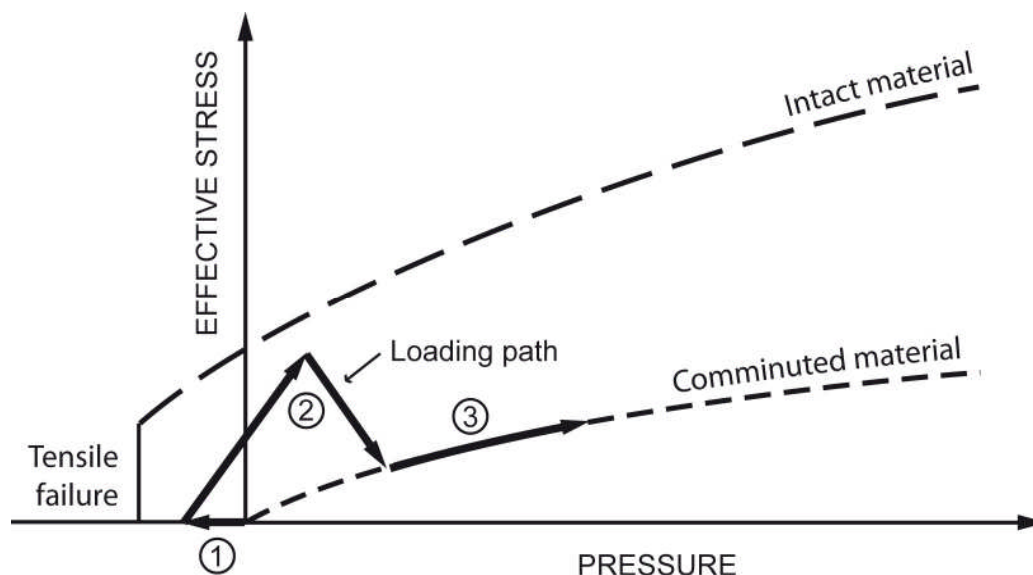


Figure 12. Strength of intact and comminuted glass and the stress path experienced by glass during penetration.

SUMMARY

Post-test examination of glass targets partially penetrated by a projectile rod suggests that target material in advance of the projectile is densely fractured into micron-sized fragments, which are extruded into more coarsely cracked target material around the projectile. Glass fragments score the nose and shaft of the projectile as it penetrates, generating frictional heat that softens and perhaps melts the glass. These observations and the data being generated on fragment sizes, shapes, and flow behavior are the basis of a computational model presented later in this conference.¹⁴

ACKNOWLEDGMENTS

This work was funded by the U.S. Tank Automotive Research, Development and Engineering Center under subcontract from Southwest Research Institute. The authors are grateful to D. W. Templeton of TARDEC and C. E. Anderson, Jr. of SwRI and their teams, for their interest and support.

REFERENCES

- ¹ S. Chocron, C.E. Anderson, Jr., and A.E. Nicholls, Constitutive Model for Borosilicate Glass and Application to Long-Rod Penetration, 23rd Int. Symp. Ballistics, **2**, 1073-1081, Gráficas Couche, Madrid, Spain (2007).
- ² S. Chocron, K.A. Dannemann, J.D. Walker, A.E. Nicholls, and C.E. Anderson, Jr., Constitutive Model for Damaged Borosilicate Glass under Confinement, *J. Am Cer. Soc.*, **90**(8), 2549-2555 (2007).
- ³ S. Chocron, K.A. Dannemann, J.D. Walker, A.E. Nicholls, and C.E. Anderson, Jr., Analytic Model of the Confined Compression Test Used to Characterize Brittle Materials, *J. Appl. Mech.*, accepted for publication (2007).
- ⁴ B. Lawn and T.R. Wilshaw, Review of Indentation Fracture: Principles and Applications, *J. Mater. Sci.*, **10**, 1049-1081 (1975).
- ⁵ A.G. Evans, Impact Damage in Ceramics, p. 302 in *Fracture Mechanics of Ceramics*, Vol. 3, Edited by R.C. Bradt, D.P.H. Hasselmann and F.F. Lange, Plenum Press, New York (1978).
- ⁶ K.C. Dao, D.A. Shockey, L. Seaman, D.R. Curran and D.J. Rowcliffe, Particle Impact Damage in Silicon Nitride, SRI Annual Report, Part III, to the Office of Naval Research, Arlington, VA, N00014-76-C-0657 (1979).
- ⁷ A.G. Evans and T.R. Wilshaw, Quasi-Static Solid Particle Damage in Brittle Solids - I. Observations, Analyses and Implications, *Acta Metallurgica*, **24**, 939-956 (1976).
- ⁸ A.G. Evans, M.E. Gulden and M. Rosenblatt, Impact Damage in Brittle Materials in the Elastic-Plastic Response Régime, *Proc. R. Soc. Lond. A*, **361**, 343 (1978).
- ⁹ D.A. Shockey, K.C. Dao, L. Seaman and D.R. Curran, Nucleation and Growth of Cracks in CVD ZnS Under Particle Impact, SRI Annual Report, Part II, to the Office of Naval Research, Arlington, VA, N00014-76-C-0657 (1979).
- ¹⁰ D.A. Shockey, A.H. Marchand, S.R. Skaggs, G.E. Cort, M.W. Burkett and R. Parker, Failure Phenomenology of Confined Ceramic Targets and Impacting Rods, *Int. J. Impact Engng.*, **9**, 263-275 (1990); also in *Ceramic Armor Materials by Design*, Eds. J.W. McCauley, A. Crowson, W.A. Gooch, A.M. Rajendran, S.J. Bless, K.V. Logan,

M. Normandia and S. Wax, *Ceramic Transactions 134*, The American Ceramic Society, 385-402 (2002).

¹¹R.W. Klopp and D.A. Shockey, The Strength Behavior of Granulated Silicon Carbide at High Strain Rates and Confining Pressure, *J. Appl. Phys.*, **70**, 7318-7326 (1991).

¹²J. Mescall and C. Tracy, Improved Modeling of Fracture in Ceramic Armor, Proceedings of the 1986 Army Science Conference, U.S. Military Academy, West Point, June 17-20 (1986).

¹³J. Mescall and V. Weiss, Materials Behavior Under High Stress and Ultra-high Loading Rates-Part II, Proceedings of the 29th Sagamore Army Conference, Army Materials and Mechanics Research Center, Watertown, MA (1984).

¹⁴D.R. Curran, D.A. Shockey and J.W. Simons, Mesomechanical constitutive relations for glass and ceramic armor, presented at the 32nd International Conference and Exposition on Advanced Ceramics and Composites (ICACC), Daytona Beach, Florida, Jan. 27-Feb. 1 (2008).

SECTION III: FLOW BEHAVIOR OF GLASS AT THE TIP OF A PENETRATOR

D. A. Shockey, D. Bergmannshoff, D. R. Curran, and J. W. Simons
Center for Fracture Physics, SRI International
Menlo Park, CA, USA

ABSTRACT

Projectiles penetrate glass armor by comminuting material at the advancing tip and forcing the fragments to flow out of the projectile path. Thus, fracture and fragment flow resistance of the glass under high pressure and shear stress control armor penetration. This paper describes a test to observe and measure the shear response of glass powder in a stress environment that simulates conditions in front of a penetrator. The data and observations provide a basis for developing physics-based models useful for computational simulations of penetration scenarios.

INTRODUCTION

The response of transparent armor to projectile attack cannot currently be computed with confidence.¹⁻³ One reason is the lack of an adequate mathematical description of the failure processes occurring in the target material under high pressure and shear. Because it is difficult to generate a physics-based model, simulations typically use models from computer libraries that capture some of the important response mechanisms with values for model parameters that are selected to provide agreement with specific ballistic test data. When models and model parameters are chosen to achieve a match with the specific results they are intended to predict, they cannot be relied on to predict the outcome of arbitrary ballistic scenarios.

To have general applicability, computational simulations require a model that describes the failure response of the target material that is activated by projectile penetration and that controls penetration resistance. The penetration phenomenology of frictional materials was clarified in recent research.⁴⁻⁵ Sectioning of partially penetrated glass and ceramic targets revealed a highly comminuted region known as the Mescall zone (MZ) (after John Mescall, who surmised its existence from his computations)⁶⁻⁷ ahead of an advancing projectile and illustrated the mechanism of penetration. The pulverized material allows a projectile to advance by flowing laterally out of the projectile path and away from the penetrator tip. Resistance to penetration is thus provided by resistance to fracture and resistance to frictional flow of the fragments under high pressure. Thus an important step in achieving a model for use in simulations is to measure the flow resistance of MZ material and how flow is affected by fragment size and shape, pressure, and loading rate.

To characterize the response of material in the MZ, a test is needed that (1) applies high pressure and shear to a bed of fragments in contact with a projectile surface, (2) allows pressure and shear stress to be varied independently, (3) allows the specimen to be recovered after the test to examine the change in bed density and in the number, size, and shape of fragments, and (4) allows for interruption of the shear load and unloading to observe and quantify fragment geometry at various shear strains. Such a test can reveal flow mechanisms, lead to damage evolution equations, and generate data

that can be incorporated into constitutive models to achieve a failure-physics-based armor design capability. This paper describes an initial design of such a test, illustrates its use, and presents and interprets measurements of shear behavior of a bed of glass fragments as a function of pressure.

EXPERIMENTAL

Experiments were performed on G018-066 quartz glass powder obtained from Schott. Designated SM 3.5, the powder had a mean size distribution $d_{50} < 3.5 \pm 1 \mu\text{m}$ with 99% of the particles being less than $13 \mu\text{m}$. Material density was 2.2 g/cm^3 , Young's modulus was 72 GPa, and the index of refraction was 1.46.

Specimens were rings of powder about 2 mm deep with inner and outer diameters of 7.87 and 15.75 mm, respectively. The specimens were produced by pouring the powder into the annulus of the holding jig and tamping lightly to produce an even surface. Using an MTS axial-torsion machine, the specimens were loaded in combined compression and torsion by first pressing the powder with a mating steel ring to a desired normal load, then rotating the ring with respect to the specimen. The maximum normal load of 200 kN (44,000 lb) produced a normal stress on the powder of 1.37 GPa (205 ksi). Figure 1 shows a schematic of the test.

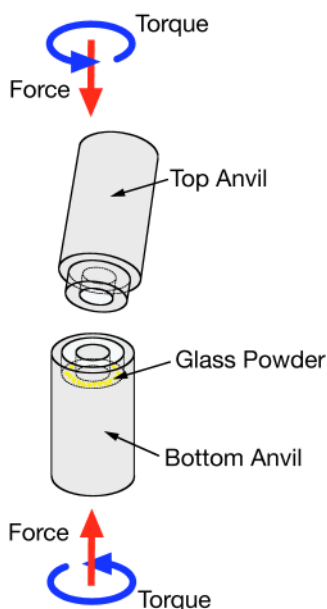


Figure 1. Specimen, holding jig, and loading mode for compressing and shearing glass powder.

Rotation angles of 10, 45, and 90 degrees produced slide distances at the center of the specimen of 1.0, 4.6, and 9.3 mm, respectively. Sliding rates were varied from 0.05 mm/s to 1.0 mm/s. Torque was measured as a function of rotational angle. Shear stresses and strains and effective friction coefficients were computed from these data and the specimen dimensions. The shear stress reported here is the average stress over the width of the annulus; average shear strain was computed by dividing slide distance by the nominal specimen thickness, about 2 mm. Especially at higher values, what is referred to

as shear strain is actually a combination of elastic shear strain in the glass particles, rearrangement and breaking up of glass particles, and sliding at the glass/metal interface.

RESULTS

Figure 2 shows shear stress as a function of shear strain under various normal forces at a displacement rate of 0.05 mm/s. At all normal forces shear stress rose monotonically with strain until reaching a maximum and then remained relatively constant for higher strains. The slopes of all curves decreased with increased shear strain. At 20 kN, the curve was smooth. For higher values of normal force, large, sudden, periodic drops in shear stress occurred, likely due to slipping at the steel-glass interface. The values for peak stress at a given normal force were consistent for repeat tests; for 8 identical tests conducted at 100 kN normal load, the measured peak stress showed a standard deviation of 6%.

The compression/torsion machine did not permit testing at ballistic rates. Stress-strain curves from tests in which the specimen was rotated 10 degrees and 90 degrees in 1 to 180 s produced shear displacement rates of from 1 to 0.05 mm/s. Results from these tests differed little, and thus rate effects in this range were small. However, for tests performed at the highest rates, the effects of the stress drops overlapped and peak values were difficult to determine from the records.

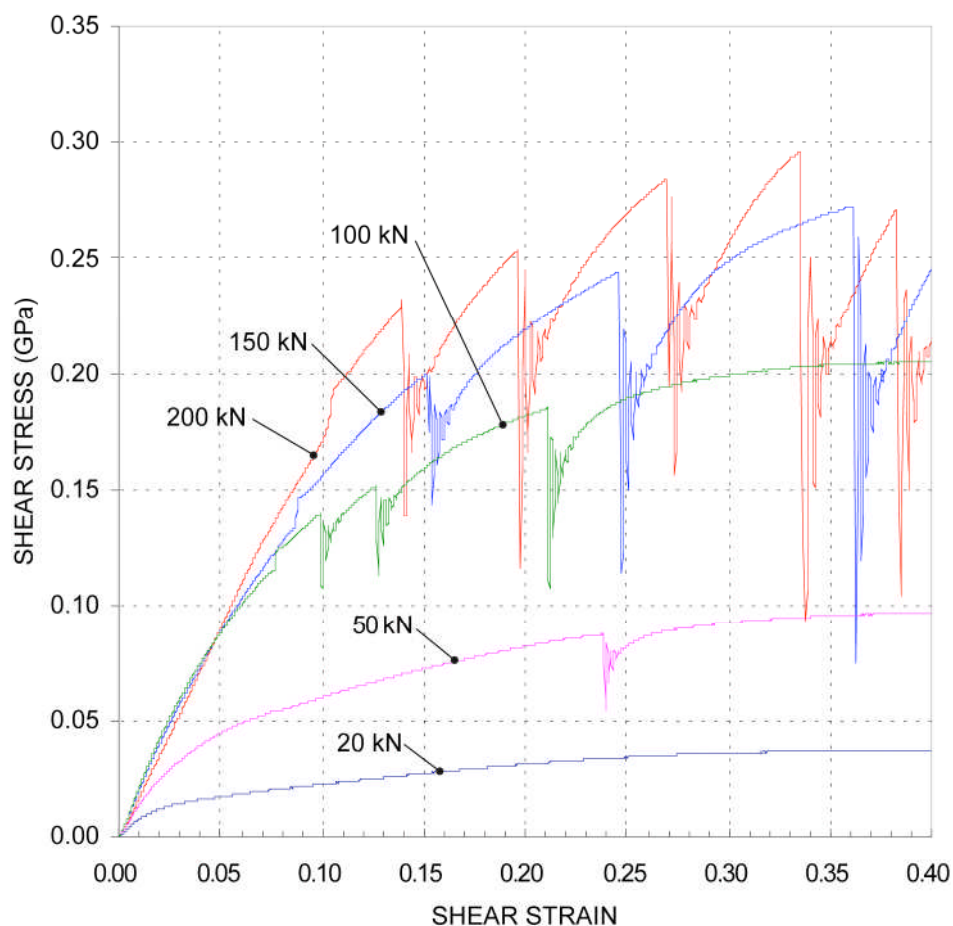


Figure 2. Shear stress vs. shear strain as a function of pressure.

POST-TEST SPECIMEN EXAMINATION

Specimens were examined post-test with optical and scanning electron microscopy to elucidate deformation and flow mechanisms and to seek explanations for the shapes of the stress-strain curves. Specimens tested at low normal loads and low shear strains remained in the initial loose-fragment state; fragments were generally straight-sided with sharp edges and roughly equiaxed, and thus had shapes similar to those of the original powder particles. At higher normal forces, shearing of the glass particles significantly altered the bed microstructure. Specimens tested at 200 kN, however, consisted of adherent aggregates of fragments (Figure 3a). The individual fragments in the aggregates tended to be less angular than those in the compressed-only powder (Figure 3b).

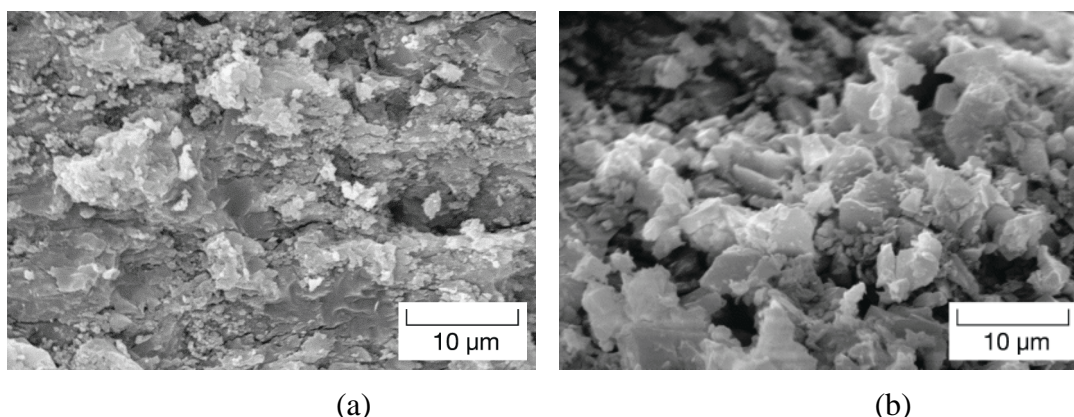


Figure 3. (a) Quartz powder after 200 kN compression followed by shear.
(b) Quartz powder after 200 kN compression only.

The fragment size distribution of selected specimens was measured with a laser-based particle classifier after the tests. Figure 4 shows the effect of normal load on the fragment size distribution for tests in which the slide distance was 9.3 mm. No change from the original size distribution was observed in tests at 10 kN and 50 kN (normal stresses of 69 MPa and 342 MPa). However, a normal load of 200 kN (1.37 GPa) narrowed and shifted the size distribution from a mean of 3.5 µm to about 2 µm, showing that larger particles were fractured and eroded.

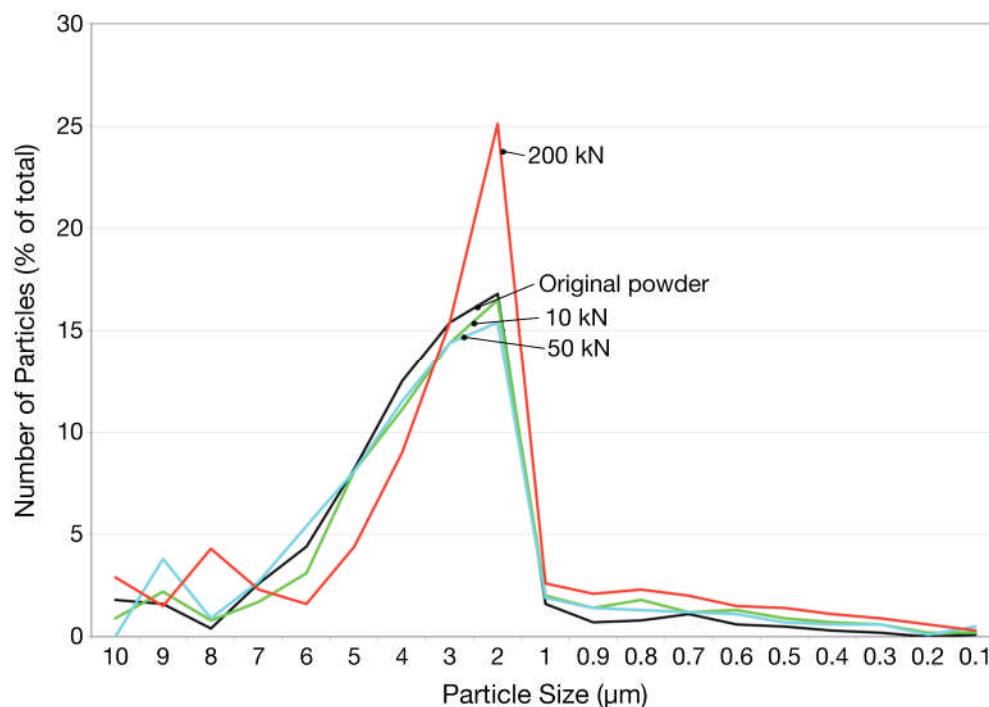


Figure 4. Size distribution of 3.5 μm quartz glass powder after testing at normal loads of 10 kN, 50 kN, and 200 kN (normal stresses of 69 MPa, 342 MPa and 1.37 GPa).

Polished cross sections through tested specimens on planes normal to a specimen radius showed cracks in two general orientations—parallel to the anvil surface, and angled at 20 to 60 degrees to the specimen axis. Left-quadrant cracks in Figure 5 formed before the right-quadrant cracks, since right-quadrant cracks terminate at the left-quadrant cracks. The cracks may have propagated intermittently, arresting and reinitiating numerous times before reaching other cracks or specimen boundaries. It is not known if the cracks were produced upon unloading or by sectioning and polishing.



Figure 5. Polished cross section normal to the specimen radial direction showing cracks.

The surfaces of the glass specimens in contact with the steel anvils were smeared and cracked (Figure 6), attesting to the sliding of the steel anvil on the glass. The directionality of the smear markings and crack profiles indicate a left-to-right movement

of the anvil on the glass surface. The dried-lake-bed cracking pattern suggests a discontinuous sliding process, where adherence between glass and steel suddenly was overcome in a local area and the area was suddenly displaced.

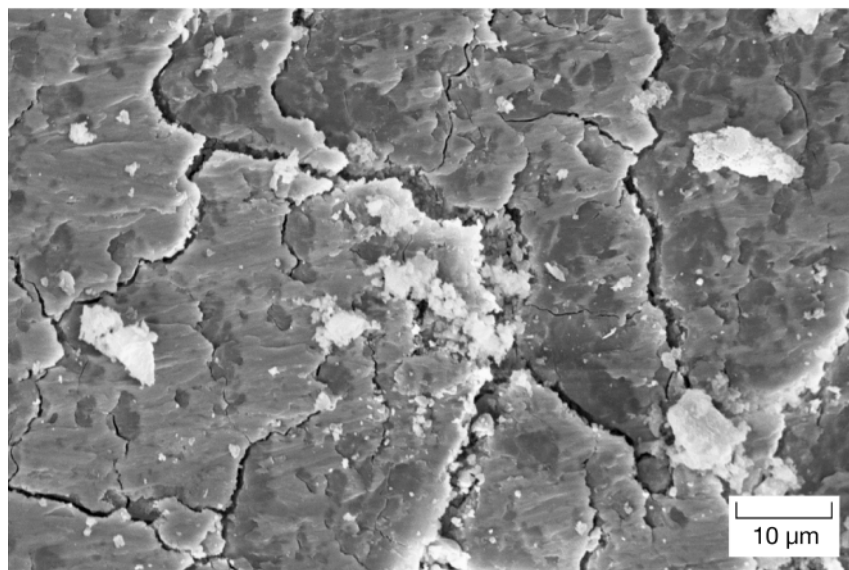


Figure 6. Surface of glass specimen next to steel anvil showing smear markings and interface stick/slip evidence.

These post-test observations indicate four mechanisms of shear flow and suggest the following explanation for the shapes of the curves in Figure 2.

For initial small strains the slope of the stress-strain curve probably measures the elastic shear stiffness of the bed of fragments as they deform in shear, but do not move. As the shear stress becomes higher, other mechanisms come into play that decrease the stiffness but may increase the strength of the bed. One mechanism is movement of the particles, leading to shear-enhanced consolidation; shear strain is taken up by individual fragments moving into adjacent interstices. As particles move, the interstitial spaces likely become fewer and smaller and the individual fragments increasingly lock up, requiring higher stress to shear the bed.

Under still higher normal loads, a second straining mechanism, particle comminution, becomes active. The larger particles that break and have their corners and edges broken off enhance the particles rearrangement mechanism, because the new smaller particles can fit into smaller interstices.

A third mechanism for accommodating shear strain is slippage between specimen and anvil. When the shear strength of the bed exceeds that of the specimen/anvil interface, bed deformation ceases and subsequent shearing occurs by sliding of the anvil over the fragment bed. Glass particles at the anvil interface are initially in point contact and, hence, present a small effective contact area over which friction can act. As shear stress is increased, frictional strength is overcome and these contact areas slip, resulting in measurable shear strain and a flattening of the stress/strain curve, but also increasing the contact area and hence requiring higher shear stress for the next increment of

displacement. Thus, even at low shear stresses and strains, the specimen/anvil interface can slip as particles adjacent to the interface rearrange.

The load drops that become more prevalent at high shear stresses and normal loads are predominantly due to interface stick slip. The phenomenon is clearly audible during the tests. At shear strains above 0.25, the average shear stress is nearly constant as the steel anvil slides over the compacted fragment bed. The load drops are manifestations of periodic stick-slip at the bed/anvil interface. Based on the peak shear stresses at the different values for normal stress, the measured coefficient of friction between glass and steel was 0.56 and independent of normal load for normal loads of 10 kN to 150 kN. At 200 kN the indicated friction coefficient was about 20% lower. The contribution to load drops from shear cracking in the specimens will be investigated in future tests in which specimens are subjected to progressively higher loads in the rising portion of the curves, then unloaded and examined microscopically.

DISCUSSION

The test described here has provided insight into the flow behavior and quantitative measurements of response for finely fragmented material in advance of a projectile penetrating a glass target. However, the test does not replicate the temperatures, rates, and pressures imposed by a penetrating projectile.

Our fractographic examinations of partially penetrated glass blocks show that temperatures get high enough to melt a thin layer of glass adjacent to the penetrator and leave a residue of steel on the glass surface.⁴ Solidified droplets and streaks of glass are observed on penetrator shafts, and previously softened and smeared glass sheet-like remnants are observed adhered to the penetrator nose. These observations suggest elevated local temperatures.

A second difference is rate. The maximum sliding rate of the test, 1 mm/s, is several orders of magnitude less than that produced by a penetrator in MZ material. Third the maximum pressure produced in the test was 1.37 GPa, whereas pressures ahead of an advancing projectile may be several times this, depending on velocity. Finally, the tests are performed on beds of loosely poured fragments and thus the specimens differ in density and packing from the initially tight in-situ fragment beds at the tip of an advancing penetrator. However, the specimens may represent fragment packing configurations in the tunnel region alongside the projectile.

The annular holding devices do not fully contain the fragments making up the specimens, allowing material to “leak out” during the test. Therefore “material properties” representative of the fragment beds are not measured. However, because the specimen geometry is identical, these edge effects are similar for all specimens and the trends in shear resistance with sliding distance, pressure, fragment size distribution, and rate are probably reliable.

The stresses measured at large (> 0.4) strains are indications of the glass-steel interface friction and hence may be useful to the modeler in describing the flow of glass fragments along the penetrator nose. However, observations of fragments in this location in partial penetration experiments indicate that the penetrator shaft is hot and the fragments are softened and even melted.⁴ Thus, friction coefficients measured here may not be characteristic of projectile penetration conditions.

SUMMARY

A test was developed to simulate the pressure/shear load conditions experienced by Mescall zone material ahead of a penetrator advancing in a glass target. The test was applied to beds of glass fragments to observe changes in bed microstructure and fragment geometry, deduce the mechanisms of flow, and measure shear resistance as a function of normal load (pressure). Shear resistance of quartz glass increased monotonically with increasing normal force until it reached a constant maximum dictated by friction at the glass/steel interface. Frequent, sudden, periodic load drops were prevalent throughout the tests, suggesting continuous flow and stick/slip of the glass on the steel anvil. The measured stress/strain relationships, their dependence on normal load, and the glass-steel coefficient of friction are data that can be used in developing physics-based models of material behavior and, hence, in computationally simulating penetration scenarios for glass armor.

ACKNOWLEDGMENTS

This work was performed for the Tank Automotive Command under subcontract to the Southwest Research Institute. The authors are grateful for the interest and support of Dr. Douglas Templeton and Dr. Charles Anderson and their staffs.

REFERENCES

- ¹G. Johnson and T. Holmquist, Some Preliminary Constitutive Models for Glass Subjected to High-Velocity Impact, Proceedings of the 32nd International Conference on Advanced Ceramics and Composites, Eds T. Ohji and A. Wereszczak, Amer. Ceram. Soc., Wiley & Sons (2008).
- ²Anderson, C. E., Presentation at the 32nd International Conference on Advanced Ceramics and Composites, (ICACC) Daytona Beach, FL (January 2008).
- ³S. Chocron, C. E. Anderson, K. A. Dannemann, and A. E. Nicholls, A Preliminary Mohr-Coulomb Model for CTH to Predict Long-Rod Penetration into Borosilicate Glass, 33rd International Conference on Advanced Ceramics and Composites, Daytona Beach, FL (January 2009).
- ⁴D.A. Shockey, A.H. Marchand, S.R. Skaggs, G.E. Cort, M.W. Burkett and R. Parker, Failure Phenomenology of Confined Ceramic Targets and Impacting Rods, *Int. J. Impact Eng.* **9**(3), 263-275 (1990). See also Ceramic Armor Materials by Design, Ed. J. W. McCauley, et al., *Ceramics Transactions* **134**, 385-402 (2002).
- ⁵D. A. Shockey, D. Bergmannshoff, D. R. Curran, and J. W. Simons, Failure Physics of Glass during Ballistic Penetration, Proceedings of the 32nd International Conference & Exposition on Advanced Ceramics & Composites (ICACC), Daytona Beach, FL, (January 2008).
- ⁶J. Mescall and C. Tracy, Improved Modeling of Fracture in Ceramic Armor, Proceedings of the 1986 Army Science Conference, U.S. Military Academy, West Point (June 17-20, 1986).
- ⁷J. Mescall and V. Weiss, Materials Behavior Under High Stress and Ultra-high Loading Rates-Part II, Proceedings of the 29th Sagamore Army Conference, Army Materials and Mechanics Research Center, Watertown, MA (1984).

SECTION IV: MESOMECHANICAL CONSTITUTIVE RELATIONS FOR GLASS AND CERAMIC ARMOR

D. R. Curran, D. A. Shockey, and J. W. Simons
SRI International
Menlo Park, CA 94025

ABSTRACT

A major challenge in achieving a physics-based computational capability for designing glass and ceramic armor is a damage evolution and fragment flow model that is usable in continuum codes. We describe a model that uses microfailure and fragment flow constitutive data, show how the model links to continuum models, and compare computational results with glass penetration tests.

BACKGROUND AND PROGRAM GOALS

Improved mesomechanical constitutive relations for glass targets undergoing microscopic damage are needed for efficient design of transparent armor. The role of the mesomechanical models is to relate material failure on the microscopic level to continuum behavior, and to give guidance to continuum models that are used in hydrocodes.

Penetration of thick targets of both ductile and brittle materials occurs by the formation of a region of yielded, flowing material at the penetrator-target interface. The flow of this material allows penetration to occur. For brittle materials like glass and ceramics, the yielded material is observed to consist of fine fragments in a thin region called the Mescall zone (MZ).¹ Our goal is to construct a mesomodel that describes the microdamage evolution, i.e., the nucleation, growth, and coalescence of microcracks to form the MZ, and subsequent granular flow of the comminuted material out of the path of the advancing penetrator. Our mesomodel is empirical, and is based on observations and data from experiments designed to measure microdamage evolution and fragment flow.

In this paper we describe a proposed initial framework for a mesomodel, incorporate available data, discuss preliminary correlations of predictions with observations, and discuss future proposed experiments.

MESOMECHANICAL APPROACH

Empirically-based mesomechanical constitutive relations have been successfully developed during the past several decades to relate material failure in metals and composites to the underlying microscopic processes, thereby helping to select appropriate continuum models and resolve apparent paradoxes.^{3,4} The key to this approach has been the development of experiments for determination of “nucleation and growth to fragmentation” (NAG/FRAG) laws in a relevant volume element (RVE) for the evolution of size distributions of microscopic voids and cracks and their coalescence to form fragments, as well as the subsequent motion of these fragments.

NAG/FRAG experiments are designed to measure key properties. As summarized in the 2004 book by Kanel, Razorenov, and Fortov,⁵ these properties include flaw sites, HEL, and molecular structure. Developing such experiments for glass presents several challenges, as follows.

- Flaw sites: Whereas most brittle materials contain internal flaws that can serve as microcrack nucleation sites, high quality glass has primarily only surface flaws. This means that in uniaxial strain plate impact experiments, for example, the microdamage should be localized in a region adjacent to the impact surface.
- HEL: Glasses do not exhibit a distinct Hugoniot elastic limit in plate impact experiments, partly because of a convex downward curvature of the Hugoniot at low pressures.
- Molecular structure: At high pressures, brittle glasses become ductile. The molecular structure of glass allows densification without cracking at pressures exceeding 7-10 GPa. At such pressures, evidence of yield may vanish, and the response may be difficult to distinguish between elastic and hydrostatic.

Prior experiments have emphasized instrumented long and short rod penetration tests ranging from near the dwell transition to steady-state penetration. The measurements include x-ray or optical “snapshots” of the position of the macrocrack front, MZ front, and penetrator tail position.^{6,7} However, until recently, experiments specifically designed to yield NAG/FRAG relations for the evolution of microscopic damage were lacking. In the present paper we focus on three types of experiments that can potentially provide such information:

1. Plate impact (uniaxial strain) experiments. These experiments simulate the loading conditions on-axis under the penetrator nose during the impact shock response.
2. Partial penetration of non-eroding rods. These experiments reproduce the loading conditions near the nose of elastic penetrators at penetration rates of several hundred m/s.
3. Quasistatic material property tests, including compression-torsion tests of powders. These experiments provide basic properties of the MZ material.

To guide planning and interpretation of the above experiments, we start with a conceptual mesomodel (CMM), which will serve as an initial framework to be modified as we obtain more microdamage evolution data.

CONCEPTUAL MESOMECHANICAL MODEL

The CMM is based on modifications of the FRAGBED2 (FB2) mesomodel of non-elastic flow in brittle materials.⁸ The non-elastic flow is assumed to be totally due to elastic fragments sliding frictionally on inter-fragment interfaces, and is treated by analogy to multi-plane plasticity models based on atomic dislocation dynamics, i.e., we focus on the movement of lines of holes between the fragments, called macrodislocations (MDs), on a finite number of slip planes. The flow is inherently rate-dependent because of crack nucleation and growth rates and fragment inertia. Linear Elastic Fracture Mechanics (LEFM) is assumed to govern the microcrack nucleation, and the “fracture toughness” is a property that represents the material’s brittleness.

Micrographs of fragmented ceramics suggest that the fragmented bed is initially a jumbled array in which flow is inhibited because the fragments block each other, and the associated MDs are “pinned”. The “yield” condition in the CMM is thus an “unpinning” condition. Figure 1 is a schematic of this situation, which also illustrates the expected importance of confining boundaries.

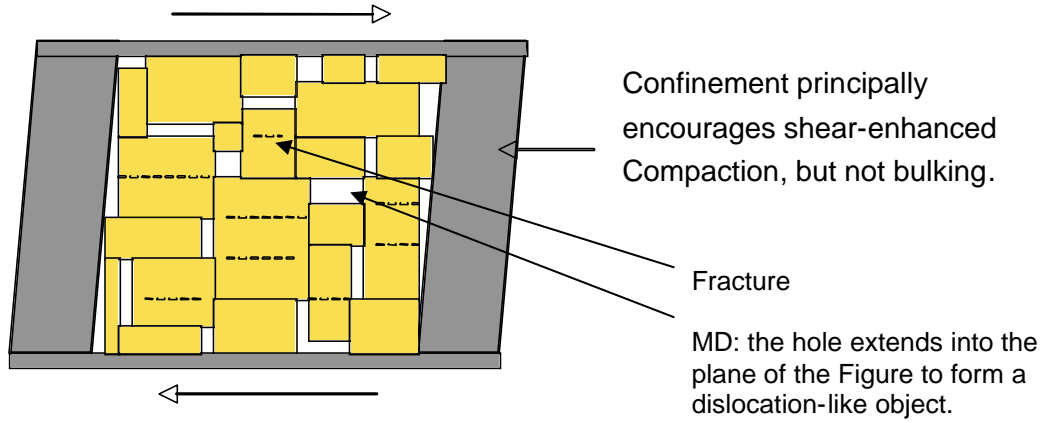


Figure 1. Schematic picture of conceptual mesomodel

The proposed unpinning criterion is based on a simplification of the FB2 comminution model. We assume that an applied remote “driving stress” state (τ , P) is sufficient to fracture fragments of size B_H or greater, given by

$$\eta B_H = \pi K_{Ic}^2 / 4 (m_1 \tau^2 + m_2 P^2) \quad (1)$$

where τ is the maximum shear stress, P is the pressure, B_H is a critical fragment size, ηB_H is the corresponding critical flaw size, K_{Ic} is the plane strain fracture toughness, and the m 's allow local stress enhancement over the remote stresses. Figure 1 shows that we idealize the fragment cross-sections as squares. An equivalent circle with the same area would thus have a radius $R = B / \pi^{1/2} = 0.56B$.

Eq (1) is clearly an oversimplified relation to be improved as more data are obtained. For example, the dynamic initiation or arrest toughness and/or a combination of Mode I and Mode II toughnesses would be more appropriate than K_{Ic} , which is used here as a simple measure of brittleness, and to show trends. We expect that a more detailed model, such as that of Simons et al⁹ for concrete and marble, may eventually be needed. As the applied stresses increase, comminution produces smaller and smaller fragments until either sufficient unpinning has occurred to allow flow, or comminution ceases because the flaw sizes are subcritical.

Specifically, we fit our data to an initial Poisson fragment size distribution

$$N_g(B) = N \exp(-B/B_0) \quad (2)$$

where $N_g(B)$ is the number of fragments per unit area of a cross section with size greater than B , N is the total number of fragments per unit area in a cross section, and B_0 is the initial average size of the fragments.⁴ The fragment density function is

$$dN/dB = (N/B_0) \exp(-B/B_0) \quad (3)$$

We assume that the initial distribution has an upper cutoff, a largest fragment, B_{\max} . We also assume that the initial hole (MD) size distribution mirrors the fragment size distribution, with the larger holes being associated with the larger fragments, and the average hole size is equal to the average fragment size. Integrating the hole area bB^2 with a density function like Eq (3) from $B = 0$ to B_{\max} gives the total initial porosity

$$\phi_T = N_H b B_O^2 [2 - f(x)] \quad (4a)$$

where N_H is the total number of holes per unit area of a cross section, b is the fraction of B that specifies the width of the hole, i.e., bB is the macroscopic Burger's vector, and

$$f(x) = (x^2 + 2x + 2)\exp(-x) \quad (4b)$$

where $x = B_{\max}/B_O$.

For a given B , say B_1 , the mobile porosity is the total porosity minus the integral from 0 to B_1 , and the ratio of mobile to total porosity is

$$\phi_M/\phi_T = [f(x_1) - f(x_2)]/[2 - f(x_2)] \quad (5)$$

where $x_1 = B_1/B_O$, and $x_2 = B_{\max}/B_O$.

For example, Eq (5) shows that when $B_1 = B_O$ and $B_{\max} = 2 B_O$, $\phi_M/\phi_T = 0.75$. That is, when the largest fragment in the distribution has been reduced to B_O , 75% of the original fragments and associated MDs have been unpinned.

For such flow to be possible, the material must contain pores (the MDs). Under the high confinement provided by the impact interface of a uniaxial strain plate impact, or on-axis at the nose of a rod impact, the MDs will tend to be driven into the confining boundary, resulting in compaction (the fragments can move into the RVE, but not out). If the confinement is maintained, the subsequent response must be elastic. This postulated behavior is shown schematically in Figure 2.

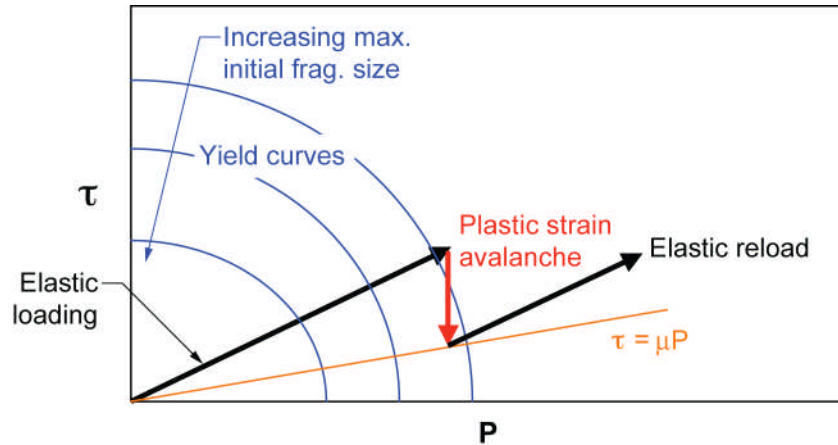


Figure 2. Postulated CMM yield behavior

The mesomodel must also describe the process by which tensile cracks and MDs (voids) are produced in originally void-free glass under compression and shear. “Wing cracks” are a candidate for causing brittle failure and dilatancy under compression and shear (see Figure 3). In general, a weak shear surface flaw can either propagate as a Mode II shear crack, or turn out of the crack plane and propagate as a wing (“splitting”) crack.

In the latter case, voids (MDs) are produced in the target, causing dilatancy. The extensive literature on this subject is reviewed in the 2004 book by Kanel, Razorenov, and Fortov⁵. Wing cracks were observed in glass plates under compression in 1963 by Brace and Bombolakis.¹⁰ Subsequent work by Nemat-Nasser and Horii,¹¹ Horii and Nemat-Nasser,¹² Moss and Gupta,¹³ and Nemat-Nasser and Obata,¹⁴ among others, described expected behavior under different stress states. Kalthoff¹⁵ performed experiments with an edge impact technique on a number of ductile and brittle materials, and found that the mode chosen depended on whether there was a mechanism for shear softening (e.g. adiabatic heating) sufficient to stabilize a propagating shear crack.

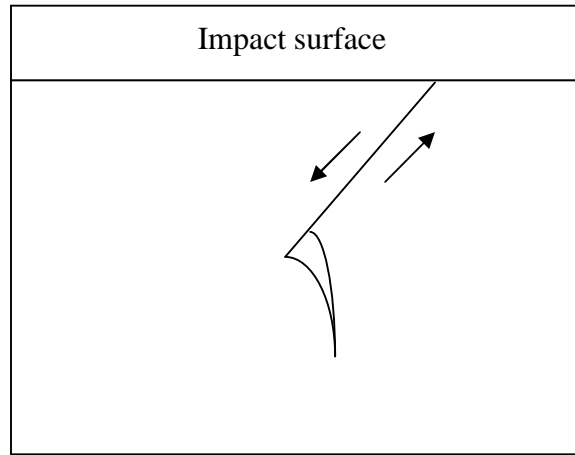


Figure 3. Wing crack

Thus, wing cracks appear to be a possible source for driving voids (MDs) into previously non-porous glass in plate impact tests. However, the brittle-ductile transition discussed above may suppress their formation, in which case we would expect a non-porous layer of damage at the impactor-target interface. To resolve this and other issues, we need more data.

SUPPORTING EXPERIMENTS

Uniaxial strain plate impact response:

We begin by examining the response of Soda-Lime Glass (SLG) samples loaded by uniaxial strain impacts in experiments reported by Simha and Gupta,¹⁶ and Alexander et al.¹⁷ We assume that cracks (wing cracks or shear cracks), originate from a size distribution of flaws of size δ on the impacted surface. We also assume that the distribution is of the form of Eq (2). To relate the flaw size to the fragment size B , we draw on the “crack range” concept of the BFRAC model for tensile cracks,⁴ which defines a parameter $M = B/\delta$. For very brittle materials, M can be between 10 and 20. The FB2 comminution model assumes that each fragment contains a flaw of size $\delta = \eta B$. Thus, $M = 1/\eta$.

For each active slip plane, Eq (1), with δ set equal to the minimum flaw size, describes the Fig. 2 yield function in $\tau - P$ space. When an elastic load path crosses the surface, the model produces a burst of non-elastic strain as the porosity is driven into the impactor surface. The shear stress drops at constant pressure to the “failed” curve $\tau = \mu P$.

To describe the non-elastic flow of the “yielded” material in a manner that ensures stability and uniqueness, an analysis due to Whitham^{18,19} is applied, and a “stress-relaxing solid” relation is used to describe the total strain rate on a slip plane as the sum of the elastic strain rate and the non-elastic strain rate:

$$\partial \epsilon / \partial t = (1/2G) \partial \tau / \partial t + \partial \epsilon^{ne} / \partial t \quad (6a)$$

where the non-elastic strain rate is given by

$$\partial \epsilon^{ne} / \partial t = [\phi / 2(2b)^{1/2} B][(\tau - \mu P) / \rho]^{1/2} H(\tau - \mu P) \quad (6b)$$

and where G is the shear modulus, H is the Heaviside function, τ is the maximum shear stress ($= \sigma_{eq}/2$), μ is the intergranular friction coefficient, ϕ is the mobile (unpinned) porosity associated with the MDs, B is the average hole (MD) height (equal to the average fragment size), and b is a dimensionless parameter that characterizes the average MD width. The quantity $[\phi / (b)^{1/2} B]$ can be considered a meso-parameter that specifies, for a given stress state on a given slip plane, both the porosity carried by a MD and the MD speed. It has significant leverage on the predicted behavior, and we will vary it in a parameter study.

In Table 1, we list measured and assumed material properties for the Soda-Lime Glass (SLG), and compare them with those for B_4C , a ceramic for which a clear two-wave response has been measured.²⁰ The glass and B_4C data warrant continued study, since both sets of experiments were well-instrumented, and give an opportunity to study the effects of different microstructures, fracture toughnesses, and moduli.

Table 1. Properties for SLG and B4C

PROPERTY	SLG	B4C
Density (g/cc)	2.5	2.51
C_L (km/s)	5.761	13.7
C_S (km/s)	3.437	8.7
C_{BULK} (km/s)	4.176	9.3
ν (Poissons ratio)	0.224	0.162
G	12 MPa* (29.5 GPa)	190 GPa
K	17 MPa* (43 GPa)	218 GPa
E	29 MPa* (73 GPa)	
K_{Ic} (MPa-m ^{1/2})	0.9	4
HEL (GPa)	3.5 – 7	16.15
Flaw locations	Surface	Surface and internal; grain boundaries, inclusions, etc.
Assumed meso properties, μ , η , B_1 , B_0 , B_{max} , $\phi/b^{1/2}B_0$	0.3, 0.1, 1 μ m, 50 μ m, 100 μ m, 10 -100 cm ⁻¹	

**The reported¹⁷ ambient pressure elastic moduli measured by ultrasound are inconsistent with the measured wave speeds, and have been corrected. The corrected values are given in the parenthesis.*

We do not have measurements of the surface flaw distributions in the glass, but we will do an example analysis assuming the mesomechanical properties listed in Table 1, including setting $B_1 = 1 \mu$ m, $B_0 = 50 \mu$ m, and $B_{max} = 100 \mu$ m. We next apply the simplified flow model of Eq (6b). To convert the τ relations to those for the longitudinal stress, S , we use the uniaxial strain conditions:

$$\tau = [3(1-2\nu)/2(1+\nu)] \quad P = P/\psi, \text{ where } \psi = [2(1+\nu)/(3(1-2\nu))], \text{ and } S = [2(1-\nu)/(1-2\nu)]\tau \quad (7)$$

Operating on Eq (6a) with $\partial/\partial t$, combining with the equations for conservation of mass and momentum, and using the above uniaxial strain relations connecting S and τ via Poisson's ratio ν , leads to

$$\partial^2 S / \partial t^2 - C^2 \partial^2 S / \partial h^2 + \lambda (\partial S / \partial t) = 0 \quad (8)$$

where h is the Lagrangian distance into the target, C is the longitudinal wave speed,

$$\lambda = (1/T) = [(1-2\nu)/2(1-\nu)]^{1/2} [1-\mu\psi]^{1/2} [0.18\phi/b^{1/2}B]\rho^{1/2}C^2S^{-1/2} \quad (9)$$

and $\psi = [2(1+\nu)/(3(1-2\nu))]$.

Using the glass values of Table 1 yields values of T = ranging from 50 to 500 ns, depending on the choice of $\phi/b^{1/2}B_0$.

Eqs (8) and (9) fulfill a stability criterion due to Whitham.^{18,19} If $\lambda \geq 0$, the solution to Eq (8) for $S(h,t)$ is well-posed and stable (dissipative). The result is a decaying elastic wave followed by a diffusive failure wave. In the linear approximation, S is given by

$$S \approx S_0(t-h/C)\exp[-\lambda h/2C] \quad (10)$$

where S_0 is the impact stress. Thus, the width of the MZ is approximately $2CT$. λ in Eq (9) is not a constant, but depends on the stress to the $-1/2$ power, thereby violating the linear assumption. However, the “viscous” overshoot from the HEL is small, so we will roughly approximate the response by setting S equal to the HEL value.

We now focus on specific experiments with SLG glass performed by Simha and Gupta [14] and Alexander et al [15], in which SLG impactors on SLG targets generated elastic impact stresses of 4 to 10 GPa at the impact surface. Both measured loading times to 4 GPa of about 0.2 μ s. For impact stresses of 4 to 6 GPa, Simha and Gupta measured a two-wave structure. For example, at 4.6 GPa, they measured a slightly rounded longitudinal stress plateau at 4 GPa, followed after about 2 μ s by a second rise to 4.6 GPa. This can be combined with their lateral stress history record to show a strength, τ , that jumps to a plateau of about 1.5 GPa, but after about 0.5 μ s, drops to about 1 GPa, only to ramp up again at about 2.5 μ s to a new plateau of about 1.5 GPa at about 3 μ s. This observed two-wave structure was interpreted by Simha and Gupta as a time-dependent loss of strength followed by a partial regaining of that strength, consistent with the CMM picture. In contrast, Alexander et al did not record a two-wave structure.

Simha and Gupta developed an ad hoc continuum strength model that correlated well with the above experiments, has similar features as the CMM model, and can therefore serve as a test of the CMM model's validity.

To further compare the CMM predicted trends with the above data, we arbitrarily set $m_1 = m_2 = 1$, and choose the parameters in Table 1 to enforce a value of 4 GPa for the HEL. The values in Table 1 for SLG give a uniaxial strain loading path of $\tau = 0.68P$. Eq (1) gives a yield circle with a radius = 2.5 GPa, corresponding to S (HEL) = 4 GPa, as desired.

The CMM model calculates a diffusion front pseudovelocity obtained by analogy to heat flow calculations,⁴ where calculations of heat flow from a hot slab, maintained at

constant temperature, suddenly placed in contact with a cold material, showed that the pseudovelocity of propagation of one-fourth the hot slab temperature, was $3k/h$, where k is the diffusivity. Taking the diffusivity to be equal to $C^2 T$, and setting the pseudovelocity equal to $h(\text{diffusion})/t$ yields

$$h(\text{diffusion}) = 1.7C(Tt)^{1/2} \quad (11)$$

So far, the discussion has concerned individual slip planes, but a further consequence of the postulated “unpinning yield condition” is that many slip planes would become active simultaneously. In Figure 1, for example, the vertical slip planes would also start to slide. The fragment cross sections, schematically shown as squares, would become “rounder”, and the material would become more like a liquid. The effective coefficient of friction μ might decrease as the particles begin to roll. But if the confinement is maintained, once the MDs have flowed into the confining penetrator interface to compact the material, the subsequent reloading would be that of an elastic liquid, and the appropriate wave speed would be the bulk wave speed.

Since the CMM model has many adjustable parameters, a wide variety of responses can be predicted. We performed a preliminary parameter study by varying the value of $\phi/b^{1/2}B_0$ over the range shown in Table 1. Figure 4 shows the two extremes ($T = 50$ ns and $T = 500$ ns) for the Simha and Gupta experiment, which produced an impact stress of 4.6 GPa. The best overall correlation is obtained with the large value of T (500 ns), which forced the diffusing failure wave to travel at almost the elastic wave speed. The slower bulk wave speed for the elastic liquid delayed the arrival of the reloading wave to about $1.6 \mu\text{s}$, in rough agreement with the Simra and Gupta results for the longitudinal stress. However, the observed regaining of strength is not predicted by the CMM (although it is possible to imagine that the fine particles compact and “freeze” to become an effective solid again).

By choosing the small value of T (50 ns), we can delay the reloading pulse to agree with the second wave arrival time recorded by Simha and Gupta. However, Figure 4 shows that the delay simply reduces the first wave to low amplitude, resulting in a poor correlation.

At higher impact stresses, the data suggest that the glass becomes ductile, undergoes densification or a phase change, and no longer behaves like a collection of elastic fragments.

Since our model predicts that the material will recompact at the impactor interface, and reload elastically, we expect that both reshocking and unloading should occur elastically, as diagrammed schematically in Figure 2. Elastic unloading was, in fact, inferred by Alexander et al.¹⁷

In summary, there are enough adjustable parameters in the CMM model to allow rough trend correlations with the plate impact data to be obtained, but we need additional damage evolution data to further constrain our model parameters. A proposed “soft recovery” plate impact experiment will be described later.

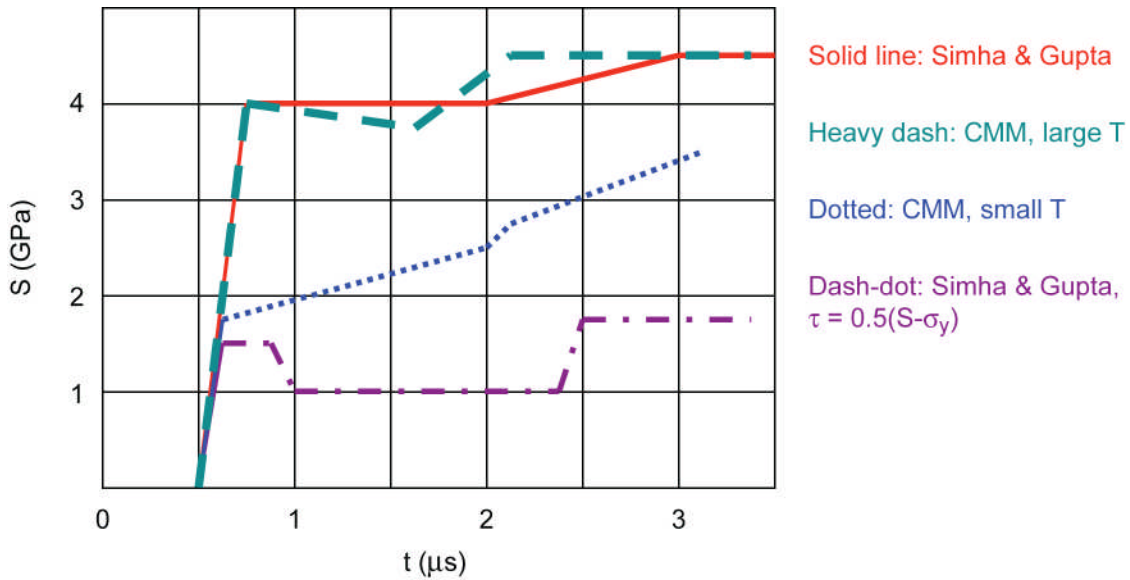


Figure 4. Comparison of CMM model trends with simplified Simha & Gupta data. Measurement is 3 mm from impact surface.

Partial penetration experiments provide valuable data under other loading conditions, and are discussed next.

Partial penetration of non-eroding rods:

As described in a companion paper in the present conference², we have performed experiments in which hard steel hemispherical-nosed rods were fired into thick, confined soda lime and borosilicate glass targets at impact velocities ranging from 300 to 600 m/s. The 6.35 mm diameter x 31.8 mm long rods remained elastic, and arrested after partial penetration. The recovered targets showed a MZ region around the penetrator that consisted of pulverized material with a fairly sharp boundary. The MZ thickness at the nose at arrest in all cases was less than 2 mm. The diameter of the tunnel ranged from about twice the rod diameter at 300 m/s impact velocity to about 4 times the rod diameter at 600 m/s impact velocity.

Finely-spaced cone cracks were driven into the target from the rod periphery as the rod advanced, and intersected with less finely-spaced lateral cracks to form a fragmented bed ranging from mm-sized fragments some distance ahead of the arrested penetrator to sub mm-sized fragments close to the boundary with the MZ, within which the fragment sizes were less than 50 microns.

The CMM model suggests the following penetration scenario. When the axial compressive stress at a given location (RVE) ahead of the penetrator reaches the critical value for the largest fragments in the RVE (Fig. 2), those fragments and MDs are unpinned, and non-elastic flow begins. At locations close enough to the penetrator/glass interface to experience significant confinement, compaction and elastic reloading occur. Still closer to the interface, a layer of elastic, compacted material attaches to the penetrator nose. A snowplow process then results in which the penetrator nose accumulates a growing, compacted layer of fine particles that attach frictionally both to each other and the penetrator.

Preliminary measurements² of the fragment size distribution in the MZ close to the penetrator's nose roughly fit a Poisson distribution with B_0 in Eq (2) equal to about 50 microns inside the MZ boundary and 60 microns outside the boundary.

If we now assume that η is 0.1 and $B_0 = 50$ microns, Eq (1) gives a critical driving stress of 0.3 GPa for the outer boundary of the MZ. This appears to correlate well with supporting hydrocode calculations at an impact velocity of 400 m/s²¹. Furthermore, the hydrocode calculations give a driving stress near the interface of about 2.5 to 3 GPa, which Eq (1) predicts will produce fragments a little less than 1 micron in size, which also correlates reasonably well with micrographs of the fragments adhered to the penetrator nose surface². In this scenario, the main role of the larger fragments in the MZ, as well as the fragments outside the MZ, is to provide the porosity that is later compacted to add to the adherent layer.

Thus, the CMM correlations are perhaps encouraging, but we again need more microdamage evolution data, as discussed next.

FUTURE TEST PROGRAM

Partial penetration tests:

The partial penetration tests fulfill the basic requirements for measuring microdamage evolution: variable load amplitudes and durations, soft-recovered specimens allowing microscopic examination of the fractured material, and recovered tunnel material for property testing. A prototype test program is described in a companion paper in this conference².

Quasistatic property tests:

Tests are needed to obtain basic material properties, especially for the pulverized material, for input to both continuum and mesomechanical models. Pressure-shear measurements on pulverized material recovered from the partial penetration tests are underway². Those tests include microstructural observations of the material before and after granular flow. We plan similar observations of damaged material from confined pressure tests being performed at SwRI. Since interaction of the pulverized material debris with the penetrator nose and sides seemed important in the partial penetration tests, we plan to also examine the material that adheres to the shear surfaces in the SwRI specimens. We will compare the evolution of fragment size and shape for the two cases.

Soft-recovered plate impact tests:

To help interpret prior plate impact data, we need tests that allow us to measure the evolution of the microdamage. In prior work on brittle tensile fracture and fragmentation in Armco iron, for example, we were able to produce different damage levels in target "pucks", and thereafter perform iterative calculations with NAG/FRAG models until we could correlate with the measured damage distributions⁴. To follow the same procedure for compression-shear loads, we need a scheme to soft-recover the target specimens for subsequent microscopic examination. A possible design is sketched in Figure 5, which shows the following features based on our earlier work^{3,4}:

- The samples are intact or pre-fractured cylindrical glass plates ("pucks").
- Impactor and confinement materials are impedance-matching aluminum alloys.

- The sample plate is surrounded by a glass collar whose purpose is to eliminate converging unloading waves, and maintain uniaxial strain in the sample for the duration of the load pulse.
- Impact velocities and transmitted stress histories are measured.
- Increasing impact velocity levels produce increasing degrees of damage.
- A standard “rag cage” is used for soft-recovery of the target package.
- The glass sample is characterized pre and post-test for fragment size, pore size, and fragment geometry distributions.

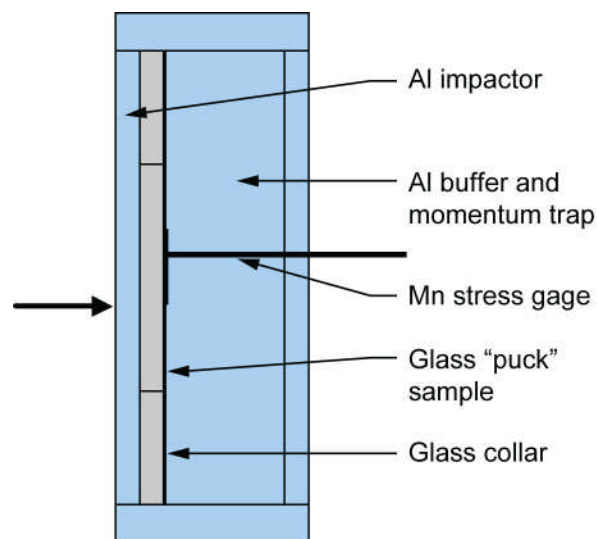


Figure 5. Plate impact test design

CONCLUSIONS

Our conceptual mesomodel (CMM) shows some promise, but needs more microdamage evolution data to improve it. As discussed above, we expect that Eq (1) will be replaced by an expression that contains static and dynamic Mode I and Mode II toughnesses and other refinements, and sophisticated crack growth and coalescence models are available for correlating better with microdamage evolution data. Some key questions are:

- How is dilatancy introduced in impacted glass targets free of internal flaws? Are wing cracks the actual mechanism? The proposed experiments of Figure 5 should help us answer that and other questions.
- What governs the sudden reduction of fragment sizes inside the MZ? The picture of “strain burst”–induced compaction followed by elastic reloading under confinement and compaction will no doubt be modified by data from the proposed additional partial penetration tests and plate impact tests.
- What are the flow properties of the material in the MZ? Data from the planned quasistatic property tests will be valuable in this area.

In general, the forthcoming detailed microscopic damage evolution data should help us replace uncertain elements of our conceptual mesomodel with empirically-determined relations.

ACKNOWLEDGMENTS

This work was funded by the U.S. Tank Automotive Command under subcontract to Southwest Research Institute. The authors are grateful to D. W. Templeton of TACOM and C. E. Anderson, Jr. and his team for their interest and support.

REFERENCES

- ¹D. A. Shockey, A. H. Marchand, S. R. Skaggs, G. E. Cort, M. W. Burkett, and R. Parker, "Failure Phenomenology of Confined Ceramic Targets and Impacting Rods", *Int. J. Impact Eng.*, **9**(3), 263-275 (2000).
- ²D. A. Shockey, D. Bergmannshoff, D. R. Curran, and J. W. Simons, "Failure Physics of Glass during Ballistic Penetration", *Proceedings of the 32nd International Conference & Exposition on Advanced Ceramics & Composites (ICACC)*, held at Daytona Beach, FL, Jan. 27 - Feb. 1, 2008.
- ³D. A. Shockey, "Rosetta Stone Experiments, and a Mesomechanical Approach to High Strain-rate Deformation and Fracture", SEM William M. Murray Lecture, *Experimental Mechanics*, DOI 10.1007/s11340-006-9030-8 (June 7, 2006).
- ⁴D. R. Curran, L. Seaman and D. A. Shockey, "Dynamic Failure of Solids", *Physics Reports*, **47**(5 & 6), March 1987.
- ⁵G. I. Kanel, S. V. Razorenov, and V. E. Fortov, Shock-Wave Phenomena and the Properties of Condensed Matter, Springer-Verlag, New York (2004).
- ⁶Th. Behner, Ch. E. Anderson Jr., D. L. Orphal, M. Wickert, V. Hohler, and D. W. Templeton, "Failure and Penetration Response of Borosilicate Glass during Short Rod Impact", *Proc. 23rd Int. Symp. Ballistics*, **2**, 1251-1258, Graficas Couche, Madrid, Spain (2007).
- ⁷C. E. Anderson Jr., T. Behner, T. J. Holmquist, M. Wickert, V. Hohler, and D. W. Templeton, "Interface defeat of long rods impacting borosilicate glass", *Proc. 23rd Int. Symp. Ballistics*, **2**, 1049-1056, Graficas Couche, Madrid, Spain (2007).
- ⁸D. R. Curran, "Comparison of Mesomechanical and Continuum Granular Flow Models for Ceramics", *Proceedings of the APS SCCM Topical Conference*, Baltimore MD, (July 31-August 6, 2005).
- ⁹J. W. Simons, T. H. Antoun, and D. R. Curran, "A Finite Element Model for Analyzing the Dynamic Cracking Response of Concrete", Presented at the 8th International Symposium on Interaction of the Effects of Munitions with Structures, McClean, Virginia (April 22-25, 1997).
- ¹⁰W. F. Brace and E. G. Bombolakis, "A Note on Brittle Crack Growth in Compression", *J. Geophys. Res.*, **68**, 3709-3713 (1963).
- ¹¹S. Nemat-Nasser and H. Horii, "Compression-induced Nonplanar Crack Extension with Application to Splitting, Exfoliation, and Rockburst", *J. Geophys. Res.*, **87**(B8), 6805-6821 (1982).
- ¹²H. Horii and S. Nemat-Nasser, "Compression-induced Macrocrack Crack Growth in Brittle Solids: Axial Splitting and Shear Failure", *J. Geophys. Res.*, **90**(B4), 3105-3125 (1985).
- ¹³W. C. Moss and Y. Gupta, "A Constitutive Model Describing Dilatancy and Cracking in Brittle Materials", *J. Geophys. Res.*, **87**(B4), 2985-2998 (1982).

- ¹⁴S. Nemat-Nasser and M. Obate, “A Microcrack Model of Dilatancy in Brittle Materials”, Trans. ASME: J. Appl. Mech., **55**(110), 24-35 (1988).
- ¹⁵J.F. Kalthoff, “Modes of dynamic shear failure in solids”, Int. J. Fracture, **101**, 1-31 (2000).
- ¹⁶C. H. M. Simha and Y. M. Gupta, “Time Dependent Inelastic Deformation of Shocked Soda-lime Glass”, J. Appl. Physics, **96**(4), 1880-1890 (August 2004).
- ¹⁷C. S. Alexander, L. C. Chhabildas, and D. W. Templeton, “The Hugoniot Elastic Limit of Soda-lime Glass”, in Shock Compression of Condensed Matter – 2007 (M. Elert, M. D. Furnish, R. Chau, N. Holmes and J. Nguyen eds., AIP Press, pp 733-738 (2007).
- ¹⁸G. B. Whitham, “Some Comments on Wave Propagation and Shock Wave Structure with Application to Magnetohydrodynamics”, Comm. Pure and Applied Mathematics, Vol. XII, 113-158 (1959).
- ¹⁹G. B. Whitham, Linear and Nonlinear Waves, John Wiley & Sons, New York (1974).
- ²⁰T. J. Holmquist and G. R. Johnson, “Characterization and Evaluation of Boron Carbide for 1D Plate Impact”, Tech. Report: SwRI Report 18.10174/03, Contract F42620-00-D-0037-BR02 (July 2006).
- ²¹C. E. Anderson, SwRI, San Antonio, TX, private communication.

UNCLASSIFIED